nature materials

Article

https://doi.org/10.1038/s41563-023-01796-7

Self-assembled soft alloy with Frank–Kasper phases beyond metals

In the format provided by the authors and unedited

Supplementary Information

Table of Contents

1. Materials and Methods

1.1. Chemical and Solvents

Trimethylsilylacetylene (Adamas-Beta, 98%), Tetrakis(triphenylphosphine) Palladium(0) ($Pd(PPh_3)_4$, Sigma-Aldrich, 99%), Copper(I) Iodide (CuI, Sigma-Aldrich, 99%), Tetrabutylammonium Fluoride (TBAF, Sigma-Aldrich, 1.0 M in THF), Copper(I) Bromide (CuBr, Adamas-Beta, 99.99%), N,N,N,N,N-Pentamethyl Diethylenetriamine (PMDETA, Adamas-Beta, 98%), 1,3,5-Tris(4-ethynylphenyl)benzene (Adamas-Beta, 97%), 1,2,4,5-Tetrabromobenzene (Adamas-Beta, 98%), Phenylboronic Acid (Adamas-Beta, 98%), Palladium(II) acetate ($Pd(OAc)_2$, Adamas-Beta, 99%), tris(o-tolyl)phosphine (TCI, 97%), Potassium carbonate (K_2CO_3, Adamas-Beta, 99.99%), [Bis(trifluoroacetoxy)iodo]benzene ($Ph(OAcF_3)_2$, Aladdin, 97%), Iodine (I_2, Greagent, 99.8%), Sodium Thiosulfate ($Na_2S_2O_4$, Greagent, 99.0%), 2,3,4,5,6-Pentabromotoluene (TCI, 98%), Potassium phosphate (K_3PO_4, Adamas-Beta, 99%), Hexaphenylbenzene (TCI), Sodium Azide (NaN_3, Acros Organics, 99%), Tetrahydrofuran (THF, Adamas-Beta, 99.9%), Toluene (Adamas-Beta, 99.5%), Dichloromethane (DCM, Greagent), Petroleum Ether (PE, Greagent), Ethyl Acetate (EA, Greagent), Chloroform-D ($CDCl_3$, Adamas-Beta, 99.8%+TMS(0.03%)). Trisilanolisooctyl POSS was purchased from Hybrid Plastics and used as received.

1.2. Characterizations

1.2.1. Nuclear Magnetic Resonance (NMR) Spectroscopy

The ^1H and ^{13}C NMR spectra were obtained in $CDCl_3$ or other solvents using Varian Mercury 500 MHz NMR spectrometer. All 1H NMR spectra were referenced to the residual proton impurities in $CDCl_3$ at $\delta = 7.26$ ppm and all ^{13}C NMR spectra were referenced to the peak of $^{13}CDCl_3$ at $\delta = 77.00$ ppm.

1.2.2. Gel Permeation Chromatography (GPC)

GPC analyses were conducted on a Tosoh HLC-8320 instrument equipped with three TSKgel columns (SuperH2000, SuperH3000, and SuperH4000) in series, a double flow type RI detector, and a UV-8320 UV detector, under an eluent flow rate of 0.6 mL/min (THF). Polystyrene standards (Polymer Laboratories) were used as the standard for molecular weight calculation.

1.2.3. Thermogravimetric analysis (TGA)

The non-isothermal decomposition experiments were carried out in a thermogravimetric analysis instrument (Model Q500, TA Instruments) in air. An initial mass of the samples used was 5 mg, scanning within the temperature range of 30 to 600 °C with a heating rate of 10 °C/min.

1.2.4. Differential scanning calorimetric experiments (DSC)

The DSC data was collected using DSC 2500 (TA Instruments, USA). An initial mass of the samples used was 3-5 mg, scanning within the temperature range of -40 to 250 °C with a heating rate of 10 °C/min.

1.2.5. Density Measurements.

The prepared sample was soaked with a water in a vial. Then, saturated potassium iodide aqueous solution was added dropwise into the vial until the sample suspended in the solution for 30 min. At this point, the density of the sample is identical with solution. The solution was then transferred into a volumetric flask. The density of the solution was calculated by weight divided by volume. The experimentally measured density of all molecules prepared in the present study is 1.05 g/cm^3.

1.3. Density functional theory (DFT) and molecular dynamics (MD) simulations

The geometry of PPP core illustrated in Figure S1 is optimized at B3LYP-D3/def2-TZVP level

with ORCA 4.1.2.[1]

All MD simulations were conducted with Gromacs 2021.5.[2] The interaction among molecules were described by the force field of optimized potentials for a liquid simulation all-atom (OPLS-AA).[3] Atomic partial charges on the molecules were estimated by the extended charge equilibration (EQeq) [4] as implemented in the open babel software. [5]

For a typical simulation of a single mesoatom with a certain number of molecules, we first stacked the molecules in a pile, with neighboring molecules twisted properly to minimize size exclusion. The mesoatom was then placed in a simulation box with dimension of 10 nm by 10 nm by 27 nm. After energy minimization, MD runs were conducted in NVT ensemble at 180 °C. During the initial 100 ps of MD simulation, pressing forces were applied to the aromatic cores of the top and bottom molecules to compress the pile of molecules. The structures reported in Figure S10 were equilibrated for 10 ns at 180 °C.

To simulate the ϕ-phase crystal formed by a certain molecule (Figure S15), mesoatom s of corresponding sizes were placed at lattice sites. Proper rotation on each mesoatom was implemented to align the mesoatom in an orientation that matches the orientation of the WS cell of the corresponding lattice site. To avoid the collapse of atoms between neighboring mesoatoms, we tacitly shrink the mesoatoms by half when packing the initial crystal. After energy minimization, the system was equilibrated for 500 ps in NVT ensemble, during which the mesoatoms recover their correct size. Following this, a production run in NPT ensemble of 10 ns was conducted. Throughout the simulation, we observed no exchange of giant molecules between adjacent mesoatoms. This stands in contrast to prior simulations that reported molecule exchange between neighboring mesoatoms.[6] Two factors, aside from the relatively brief simulation duration, may elucidate this discrepancy. Firstly, the substantial size of the giant molecules employed in our study, and secondly, the absence of solvent in our system, both potentially contribute to the lack of molecule exchange. To quantify the local environment of mesoatoms of different sizes in the ϕ-phase crystal, we calculated the interaction energy of each mesoatom with the other mesoatoms in the simulation box,

$$E_n = \frac{E_{\text{inter}}+E_{\text{intra}}}{n} - E_1.$$

Here, E_{inter} is the interaction energy between the selected mesoatom and all the other mesoatoms in the simulation box. E_{intra} is the non-bonded interaction the selected mesoatom, n is the number of molecules in the selected mesoatom, and E_1 is the interaction energy between one molecule and its environment in an amorphous melt (more details in the following paragraphs). This interaction energy is similar spiritually to the Madelung potential commonly used to characterize the local solvation environment of ions in solution. [7]

The local environment of a mesoatom in BCC phase was analyzed similarly. For a BCC-phase crystal formed by mesoatoms containing n molecules, we initially placed two n-mesoatoms at the two lattice basis points. After similar equilibration and production runs, the total non-bonded potential energy (Figure S16) in the system was divided by $2n$ to give the normalized interaction energy of a mesoatom with its environment.

1.4. Synthetic Procedures

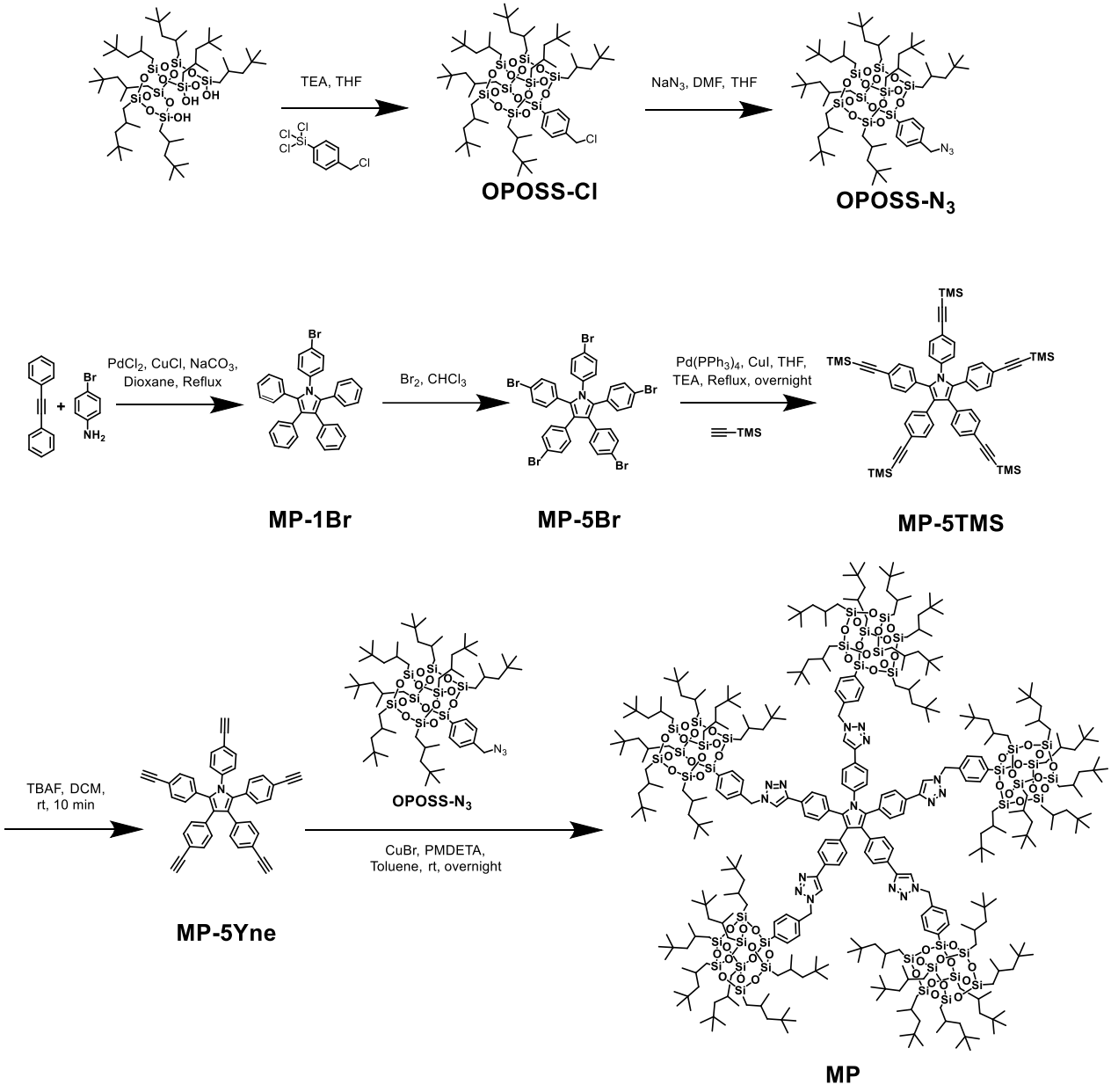

Scheme S1. Synthesis of giant molecule MP.

OPOSS-N_3 and 1,2,3,4,5-penta(4-bromophenyl)pyrrole (**MP-5Br**) were synthesized based on the procedures reported elsewhere.[8,9] Specifically, **OPOSS-Cl** was synthesized by corner-capping of Trisilanolisooctyl POSS with (p-chloromethyl)phenyltrichlorosilane in the presence of base. Subsequently, **OPOSS-N3** was derived through an azidation reaction of **OPOSS-Cl**.[8] **MP-1Br** was synthesized by Pd-catalyzed reaction of arylamines and diphenylacetylenes.[10] It was followed by a bromination reaction to yield the product **MP-5Br**. Purity of **MP** and **M1-4** was verified with GPC (Figure S20) and NMR (Figure S21-S29).

Synthesis of MP-5TMS: To the mixtures of THF (10 mL) and TEA (10 mL) in 100 mL Schlenk tube, **MP-5Br** (400 mg, 0.48 mmol) and trimethylsilylacetylene (713 mg, 7.19 mmol) were added under Ar atmosphere. Followed by adding $Pd(PPh_3)_4$ (166 mg, 0.14 mmol) and CuI (27 mg, 0.14 mmol). The mixtures were stirring at 90 °C overnight. Then solvent was removed under vacuum. the residue was purified by silica gel chromatography eluting with PE: DCM = 4:1 to give **MP-**

5TMS (230 mg, 0.25 mmol, 51.6 %) as light-yellow solid. ^{1}H NMR (500 MHz, $CDCl_3$): δ 7.24 (m, 2H), 7.18 (m, 8H), 6.78 (m, 6H), 6.74 (m, 4H), 0.24 (s, 9H), 0.23 (s, 18H), 0.22 (s, 18H). ^{13}C NMR (125 MHz, $CDCl_3$): δ 138.13, 135.20, 132.60, 131.90, 131.83, 131.78, 131.20, 131.01, 129.03, 123.31, 122.47, 121.79, 120.68, 105.61, 105.10, 104.26, 96.09, 95.44, 94.49, 31.84, 30.46, 27.24, 0.29, 0.23, 0.17.

Synthesis of MP-5Yne: To the solution of **MP-5TMS** (50 mg, 0.054 mmol) in DCM (5 mL), TBAF (212 mg, 0.81 mmol) was measured and added under Ar atmosphere. The solution was stirred for 10 minutes at room temperature. Then solvent was removed under vacuum. The residue was directly applied onto silica gel column eluting with DCM to give **MP-5Yne**. The yellow solid was used without further purification.

Synthesis of MP: To the solution of **MP-5Yne** (30 mg, 0.053 mmol) in toluene, **OPOSS-N$_3$** (500 mg, 0.37 mmol) and CuBr (5 mg) was added under Ar atmosphere, followed by adding PMDETA (100 μL). The mixtures were stirring at room temperature for 12 hours. Then the crude product was directly applied onto silica gel column with a gradient elution (gradually changed from PE to PE: EA = 4:1) to afford the desired product (280 mg, 0.0385 mmol, 72.6%) as colorless solid. ^{1}H NMR (500 MHz, $CDCl_3$): δ 7.68 (m, 10H), 7.57-7.45 (m, 15H), 7.24 (m, 10H), 6.95 (m, 10H), 5.51 (m, 10H), 1.88-0.54 (m, 5×(17×7)H). ^{13}C NMR (125 MHz, $CDCl_3$): δ 148.58, 148.14, 136.82, 136.68, 135.24, 135.19, 135.16, 132.90, 132.82, 131.89, 131.81, 131.62, 128.94, 127.94, 127.41, 127.28, 127.25, 125.53, 125.42, 124.61, 123.72, 123.06, 119.94, 119.73, 119.50, 54.23, 54.19, 54.14, 54.04, 35.23, 35.12, 34.69, 31.76, 31.68, 31.42, 31.34, 30.39, 30.29, 29.95, 29.69, 25.99, 25.94, 25.91, 25.87, 25.82, 25.24, 25.22, 25.18, 23.85, 23.82, 23.66.

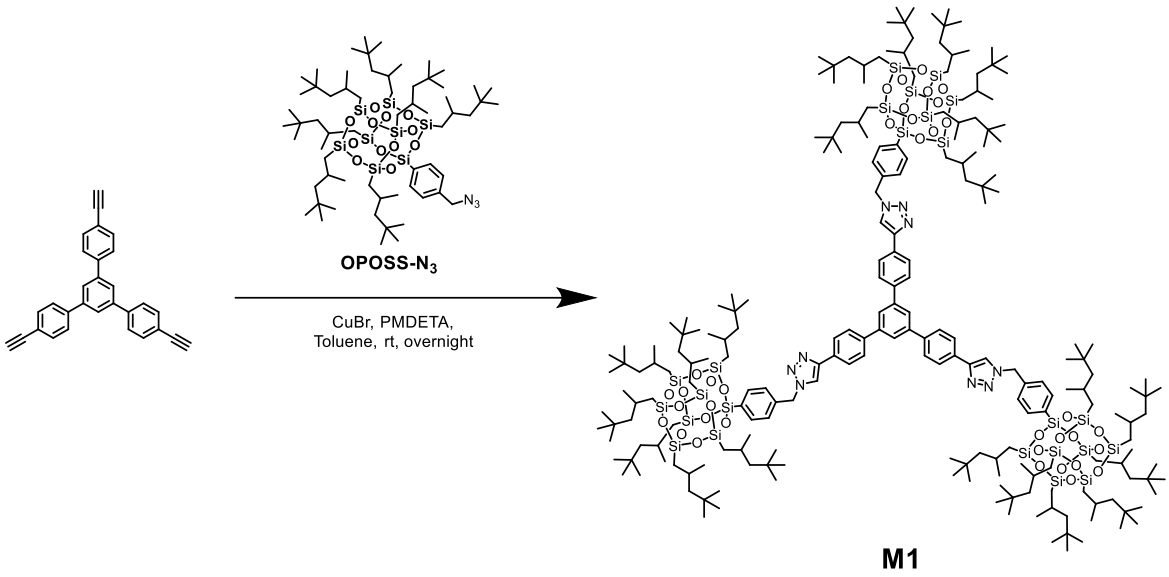

Scheme S2. Synthesis of giant molecule **M1**.

Synthesis of M1: To the solution of 1,3,5-Tris(4-ethynylphenyl)benzene (7 mg, 0.018 mmol) in toluene, **OPOSS-N$_3$** (100 mg, 0.075 mmol) and CuBr (1 mg) was added under Ar atmosphere, followed by adding PMDETA (20 μL). The mixtures were stirring at room temperature for 12 hours. Then the crude product was directly applied onto silica gel column with a gradient elution (gradually changed from PE to PE: EA = 6:1) to afford the desired product (68 mg, 0.0154 mmol, 85.8%) as colorless solid. ^{1}H NMR (500 MHz, $CDCl_3$): δ 7.91 (d, 6H), 7.82 (s, 3H), 7.75 (d, 6H), 7.72 (d, 6H), 7.68 (s, 3H), 7.31 (d, 6H), 5.51 (s, 6H), 1.88-0.54 (m, 3×(17×7)H). ^{13}C NMR (125 MHz, $CDCl_3$): δ 148.15, 142.13, 140.97, 136.73, 135.27, 133.06, 130.10, 127.97, 127.46, 126.42, 125.19, 119.75, 54.53, 54.21, 54.08, 31,41, 31.34, 30.37, 30.28, 25.86, 25.21, 23.83, 23.67.

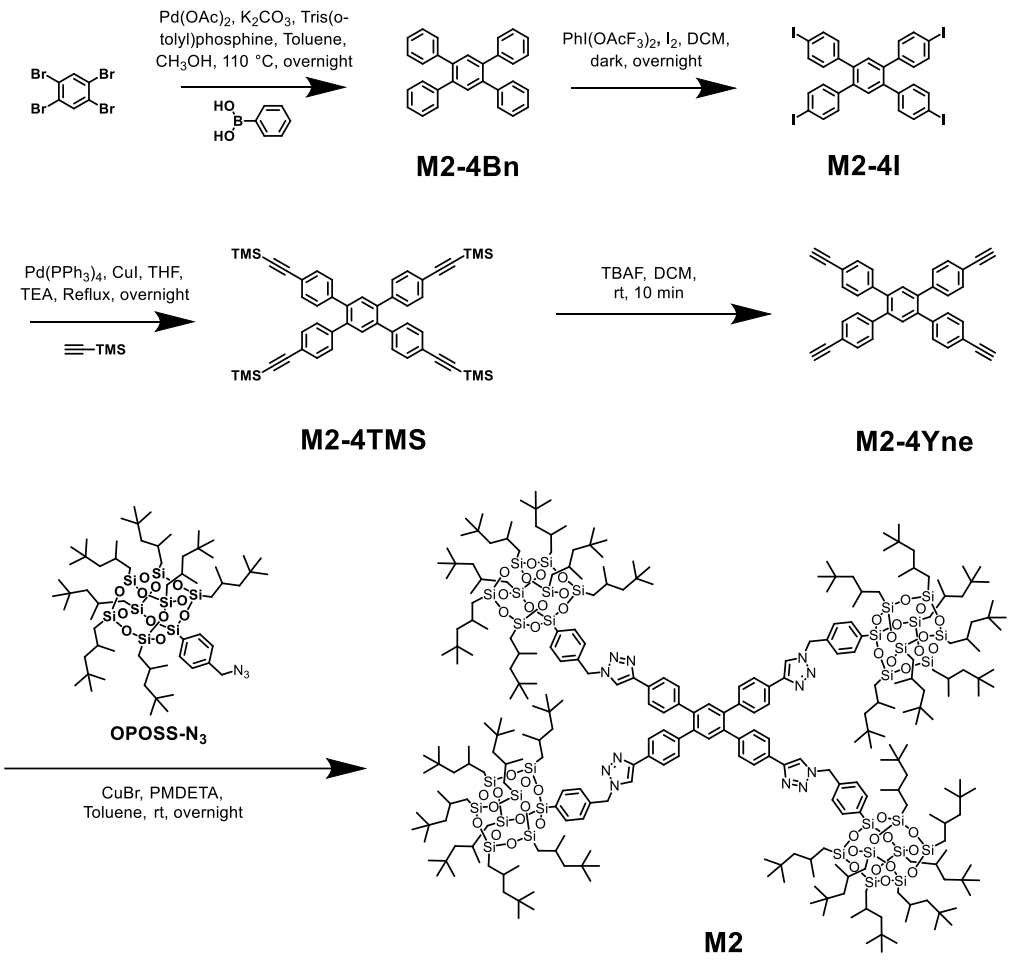

Scheme S3. Synthesis of giant molecule **M2.**

Synthesis of M2-4Bn: To the mixtures of THF (30 mL) and CH_3OH (10 mL) in 250 mL Schlenk tube, 1,2,4,5-Tetrabromobenzene (787 mg, 2.0 mmol), phenylboronic Acid (1.46 g, 12.0 mmol), tris(o-tolyl)phosphine (61 mg, 0.2 mmol) and K_2CO_3 (2.76 g, 20 mmol, in 8 ml water) were added. Then the mixture was degassed by three freeze-pump-thaw cycles, followed by adding $Pd(OAc)_2$ (22 mg, 0.1 mmol) under Ar atmosphere. The mixtures were stirring at 110 °C overnight. Then solvent was removed under vacuum. the residue was purified by silica gel chromatography eluting with PE: DCM = 1:1 to give **M2-4Bn** (653mg, 1.71 mmol, 85.4 %) as white crystals. ^{1}H NMR (500 MHz, $CDCl_3$): δ 7.55 (s, 2H), 7.24 (m, 20H). ^{13}C NMR (125 MHz, $CDCl_3$): δ 141.19, 139.89, 133.23, 130.15, 128.21, 126.88.

Synthesis of M2-4I: M2-4Bn (190 mg, 0.50 mmol), I_2 (277 mg, 1.09 mmol) and $PhI(OAcF_3)_2$ (491 mg, 1.14 mmol) were dissolved in DCM (10 ml) under Ar atmosphere. Then the mixture as stirred at dark overnight. The mixture was quenched by aqueous $Na_2S_2O_4$, and the organic layers was collected and washed with water (50 mL × 2), brine (50 mL), dried over Na_2SO_4, concentrated by rotary evaporation, and precipitated into cold hexane. The white solids were collected and dried in vacuo to afford **M2-4I** (335 mg, 0.378 mmol, 75.6%). ^{1}H NMR (500 MHz, $CDCl_3$): δ 7.60 (m, 8H), 7.39 (s, 2H), 6.92 (m, 8H). ^{13}C NMR (125 MHz, $CDCl_3$): δ 139.98, 139.09, 137.66, 132.95, 131.81, 93.29.

Synthesis of M2-4TMS: To the mixtures of THF (10 mL) and TEA (10 mL) in 100 mL Schlenk tube, **M2-4I** (200 mg, 0.23 mmol) and trimethylsilylacetylene (269 mg, 2.7 mmol) were added under Ar atmosphere. Followed by adding $Pd(PPh_3)_4$ (78 mg, 0.07 mmol) and CuI (13 mg, 0.07

mmol). The mixtures were stirring at 90 °C overnight. Then solvent was removed under vacuum. the residue was purified by silica gel chromatography eluting with PE: DCM = 5:1 to give **M2-4TMS** (100 mg, 0.13 mmol, 56.4 %) as white solid. ^{1}H NMR (500 MHz, $CDCl_3$): δ 7.45 (s, 2H), 7.34(m, 8H), 7.11 (m, 8H), 0.25 (s, 36H). ^{13}C NMR (125 MHz, $CDCl_3$): δ 140.87, 139.54, 132.80, 132.03, 129.90, 121.94, 105.11, 95.10, 0.20.

Synthesis of M2-4Yne: To the solution of **M2-4TMS** (14.5 mg, 0.019 mmol) in DCM (5 mL), TBAF (79mg, 0.81 mmol) was measured and added under Ar atmosphere. The solution was stirred for 10 minutes at room temperature. Then solvent was removed under vacuum. The residue was directly applied onto silica gel column eluting with DCM to give **M2-4Yne**. The white solid was used without further purification.

Synthesis of giant molecule M2: To the solution of **M2-4Yne** (9 mg, 0.017 mmol) in toluene, **OPOSS-N_3** (150 mg, 0.11 mmol) and CuBr (2 mg) was added under Ar atmosphere, followed by adding PMDETA (30 μL). The mixtures were stirring at room temperature for 12 hours. Then the crude product was directly applied onto silica gel column with a gradient elution (gradually changed from PE to PE: EA = 5:1) to afford the desired product (91 mg, 0.0156 mmol, 91.6%) as colorless solid. ^{1}H NMR (500 MHz, $CDCl_3$): δ 7.71 (d, 8H), 7.67 (d, 8H), 7.59 (s, 4H), 7.57 (s, 2H), 7.29 (d, 8H), 7.28 (d, 8H), 5.56 (s, 6H), 1.98-0.54 (m, 4×(17×7)H). ^{13}C NMR (125 MHz, $CDCl_3$): δ 148.17, 140.87, 139.58, 136.68, 135.23, 133.00, 130.60, 129.21, 127.44, 125.76, 119.72, 54.20, 54.07, 31.41, 31.34, 30.38, 30.29, 25.85, 25.21, 23.84, 23.67.

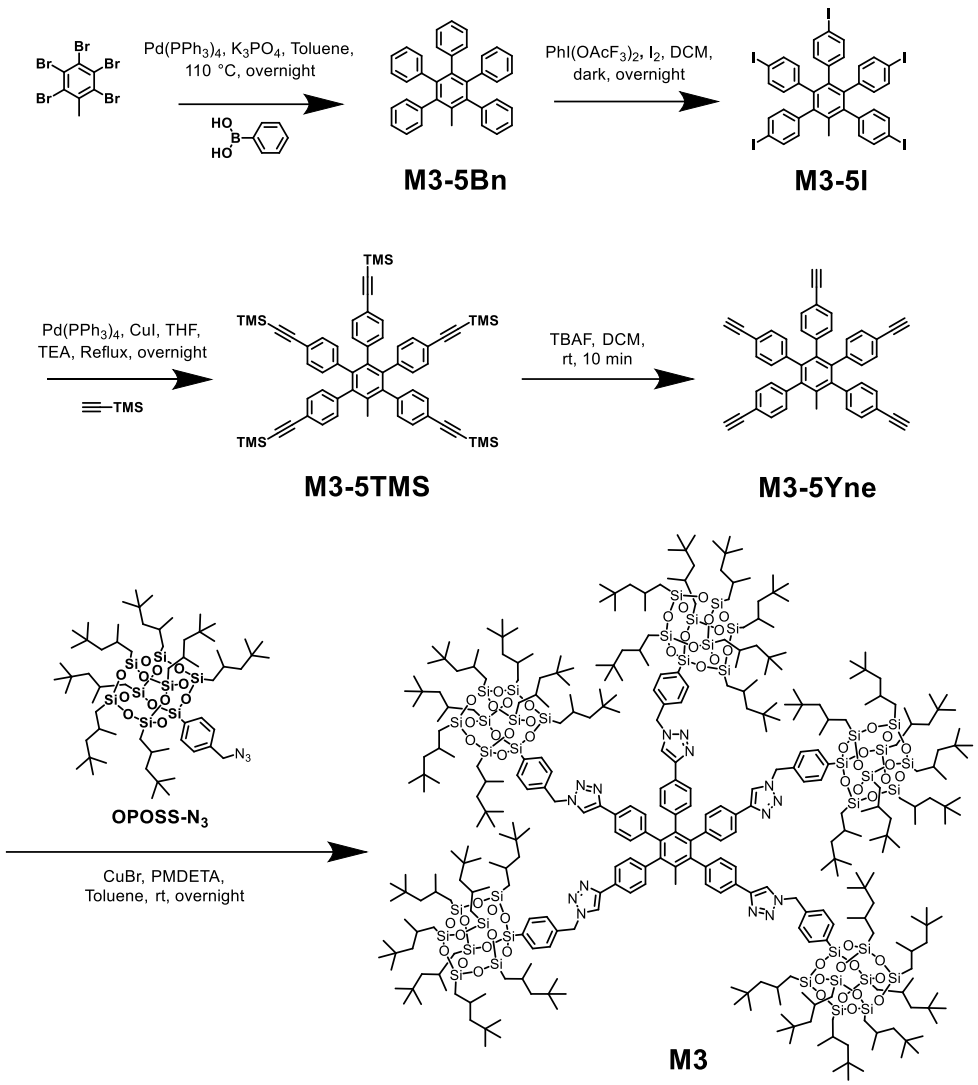

Scheme S4. Synthesis of giant molecule **M3**.

Synthesis of M3-5Bn: To the mixtures of THF (30 mL) and CH_3OH (10 mL) in 250 mL Schlenk tube, 2,3,4,5,6-Pentabromotoluene (2 g, 4.11 mmol), Phenylboronic Acid (5.5 g, 45 mmol) and K_3PO_4 (9.6 g, 45 mmol) were added to toluene (50 ml) in 250 mL Schlenk tube under Ar atmosphere. Followed by adding $Pd(PPh_3)_4$ (478 mg, 0.41 mmol). The mixtures were stirring at 110 °C overnight. After cooling to room temperature, the mixture was diluted with water and extracted with DCM. The combined organic layers were dried (Na_2SO_4), filtered and the filtrate was concentrated in vacuo. The residue was purified by column chromatography. Then solvent was removed under vacuum. the residue was purified by silica gel chromatography eluting with PE: DCM = 4:1 to give **M3-5Bn** (500 mg, 1.06 mmol, 25.8 %) as white solid. ^{1}H NMR (500 MHz, $CDCl_3$): δ 7.20-7.07 (m, 10H), 6.86-6.76 (m, 15H), 1.93 (s, 3H). ^{13}C NMR (125 MHz, $CDCl_3$): δ 141.53, 141.20, 140.90, 140.83, 140.44, 138.77, 133.73, 131.63, 131.44, 130.58, 127.72, 126.69, 126.18, 125.36, 125.30, 27.15, 19.90.

Synthesis of M3-5I: M3-5Bn (200 mg, 0.42 mmol), I_2 (300 mg, 1.18 mmol) and $PhI(OAcF_3)_2$ (500 mg, 1.19 mmol) were dissolved in DCM (10 ml) under Ar atmosphere. Then the mixture as stirred at dark overnight. The mixture was quenched by aqueous $Na_2S_2O_4$, and the organic layers was collected and washed with water (50 mL × 2), brine (50 mL), dried over Na_2SO_4, concentrated by rotary evaporation, and precipitated into cold hexane. The white solids were collected and dried

in vacuo to afford **M3-5I** (280 mg, 0.254 mmol, 60.5%). ^{1}H NMR (500 MHz, $CDCl_3$): δ 7.53 (m, 4H), 7.23 (m, 4H), 7.20 (m, 2H), 6.77 (m, 4H), 6.50 (m, 4H), 6.47 (m, 2H), 1.81 (s, 3H). ^{13}C NMR (125 MHz, $CDCl_3$): δ 140.50, 140.17, 139.50, 139.33, 137.27, 136.40, 133.11, 132.89, 132.14, 92.53, 92.05, 19.88.

Synthesis of M3-5TMS: To the mixtures of THF (10 mL) and TEA (10 mL) in 100 mL Schlenk tube, **M3-5I** (150 mg, 0.136 mmol) and trimethylsilylacetylene (203 mg, 2.05 mmol) were added under Ar atmosphere. Followed by adding $Pd(PPh_3)_4$ (47 mg, 0.04 mmol) and CuI (7.8 mg, 0.04 mmol). The mixtures were stirring at 90 °C overnight. Then solvent was removed under vacuum. the residue was purified by silica gel chromatography eluting with PE: DCM = 4:1 to give **M3-5TMS** (41 mg, 0.043 mmol, 31.7 %) as white solid. ^{1}H NMR (500 MHz, $CDCl_3$): δ 7.29 (m, 4H), 6.98 (m, 8H), 6.94 (m, 2H), 6.71 (m, 4H), 6.68 (2, 8H), 1.79 (s, 3H), 0.23 (s, 18H), 0.20 (s, 18H), 0.19 (s, 9H). ^{13}C NMR (125 MHz, $CDCl_3$): δ 141.26, 140.84, 140.62, 140.48, 139.71, 137.94, 134.08, 131.73, 131.19, 130.99, 130.92, 130.24, 121.25, 120.45, 120.38, 105.53, 105.28, 94.51, 94.14, 31.74, 30.37, 29.93, 19.63, 0.17, 0.15.

Synthesis of M3-5Yne: To the solution of **M3-5TMS** (12.2 mg, 0.013 mmol) in DCM (5 mL), TBAF (50.2mg, 0.192 mmol) was measured and added under Ar atmosphere. The solution was stirred for 10 minutes at room temperature. Then solvent was removed under vacuum. The residue was directly applied onto silica gel column eluting with DCM to give **M3-5Yne**. The white solid was used without further purification.

Synthesis of giant molecule M3: To the solution of **M3-5Yne** (7.6 mg, 0.013 mmol) in toluene, **OPOSS-N$_3$** (120 mg, 0.09 mmol) and CuBr (2 mg) was added under Ar atmosphere, followed by adding PMDETA (30 μL). The mixtures were stirring at room temperature for 12 hours. Then the crude product was directly applied onto silica gel column with a gradient elution (gradually changed from PE to PE: EA = 4:1) to afford the desired product (85 mg, 0.0116 mmol, 89.2%) as colorless solid. ^{1}H NMR (500 MHz, $CDCl_3$): δ 7.67 (m, 10H), 7.59 (s, 4H), 7.51 (s, 4H), 7.40 (s, 4H), 7.38 (s, 2H), 7.27 (m, 6H), 7.23 (m, 10H), 7.13 (d, 4H), 6.88 (d, 4H), 6.84 (d, 2H), 5.51 (s, 4H) , 5.44 (s, 4H), 5.42 (s, 2H) 1.87 (s, 3H), 1.94-0.53 (m, 5×(17×7)H). ^{13}C NMR (125 MHz, $CDCl_3$): δ 148.18, 136.36, 135.19, 127.49, 127.39, 124.48, 119.52, 54.19, 54.05, 31.41, 31.34, 30.38, 30.30, 30.27, 25.94, 25.90, 25.22, 25.18, 23.83, 23.65.

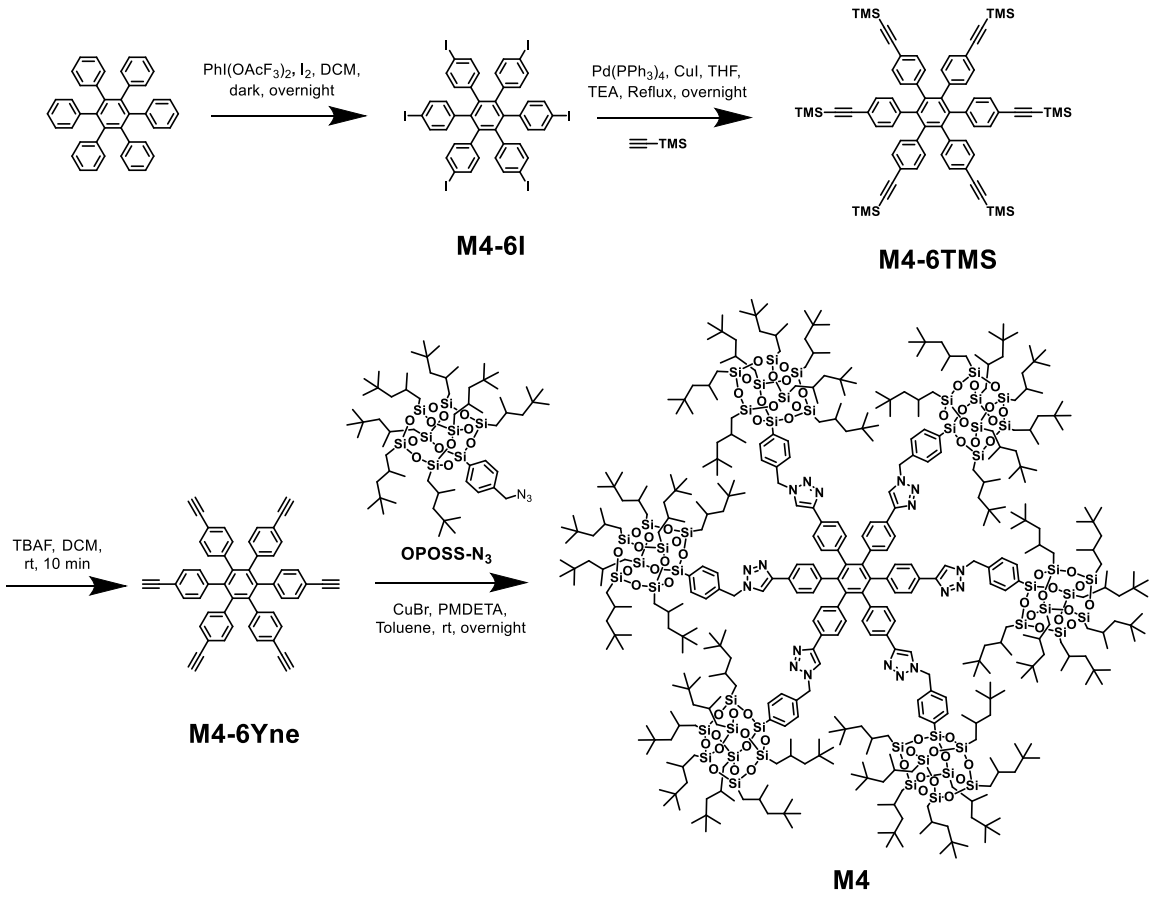

Scheme S5. Synthesis of giant molecule **M4.**

Synthesis of M4-6I: Hexaphenylbenzene (200 mg, 0.37 mmol), I_2 (210 mg, 0.82 mmol) and $PhI(OAcF_3)_2$ (354 mg, 0.82 mmol) were dissolved in DCM (10 ml) under Ar atmosphere. Then the mixture as stirred at dark overnight. The mixture was quenched by aqueous $Na_2S_2O_4$, and the organic layers was collected and washed with water (50 mL × 2), brine (50 mL), dried over Na_2SO_4, concentrated by rotary evaporation, and precipitated into cold hexane. The white solids were collected and dried in vacuo to afford **M4-6I** (310 mg, 0.24 mmol, 64.9%). ^{1}H NMR (500 MHz, $CDCl_3$): δ 7.24 (m, 12H), 6.46 (m, 12H). ^{13}C NMR (125 MHz, $CDCl_3$): δ 139.72, 139.21, 136.57, 133.03, 92.19.

Synthesis of M4-6TMS: To the mixtures of THF (10 mL) and TEA (10 mL) in 100 mL Schlenk tube, **M4-6I** (150 mg, 0.124 mmol) and trimethylsilylacetylene (222 mg, 2.23 mmol) were added under Ar atmosphere. Followed by adding $Pd(PPh_3)_4$ (57 mg, 0.05 mmol) and CuI (9.5 mg, 0.05 mmol). The mixtures were stirring at 90 °C overnight. Then solvent was removed under vacuum. the residue was purified by silica gel chromatography eluting with PE: DCM = 3:1 to give **M4-6TMS** (49 mg, 0.044 mmol, 35.5 %) as white solid. ^{1}H NMR (500 MHz, $CDCl_3$): δ 6.98 (m, 12H), 6.68 (m, 12H), 0.21 (s, 54H). ^{13}C NMR (125 MHz, $CDCl_3$): δ 140.32, 134.04, 131.15, 131.05, 120.58, 105.47, 94.34, 0.14.

Synthesis of M4-6Yne: To the solution of **M4-6TMS** (10.4 mg, 0.009 mmol) in DCM (5 mL), TBAF (44 mg, 0.168 mmol) was measured and added under Ar atmosphere. The solution was stirred for 10 minutes at room temperature. Then solvent was removed under vacuum. The residue was directly applied onto silica gel column eluting with DCM to give **M4-6Yne**. The white solid was used without further purification.

Synthesis of giant molecule M4: To the solution of **M4-6Yne** (6.35 mg, 0.009 mmol) in toluene, **OPOSS-N_3** (100 mg, 0.075 mmol) and CuBr (2 mg) was added under Ar atmosphere, followed by adding PMDETA (20 μL). The mixtures were stirring at room temperature for 12 hours. Then the crude product was directly applied onto silica gel column with a gradient elution (gradually changed from PE to PE: EA = 5:1) to afford the desired product (75 mg, 0.0086 mmol, 91.7%) as colorless solid. ^{1}H NMR (500 MHz, $CDCl_3$): δ 7.66 (d, 12H), 7.40 (s, 6H), 7.25 (d, 12H), 7.22 (d, 12H), 6.85 (d, 12H), 5.43 (s, 12H), 1.90-0.53 (m, 6×(17×7)H). ^{13}C NMR (125 MHz, $CDCl_3$): δ 148.11, 140.50, 140.36, 136.31, 135.20, 132.95, 131.92, 127.52, 124.59, 119.70, 54.37, 54.20, 54.04, 54.01, 31.41, 31.33, 30.38, 30.30, 29.68, 25.97, 25.93, 25.87, 25.24, 25.22, 25.18, 23.85, 23.66.

2. Supplementary Text

2.1. Characterization of lattice structures of μ and ϕ phase

In this section, we would present in-depth discussions on structural determination of μ and ϕ phase. The discussions include: 1. Bragg peaks in 1D small-angle X-ray scattering (SAXS) profiles. 2. Characteristic textures under bright-field transmission electron microscope (BF-TEM). 3. Lattice transition between μ and ϕ phases. 4. Unit cell reconstruction and simulation of diffraction intensity. 5. Characterization of cryo-microtomed samples. Proposed lattice structures (.cif file) of μ and ϕ phases are presented in extended data (https://doi.org/10.6084/m9.figshare.23497661.v1).

2.1.1. Bragg peaks in 1D small-angle X-ray scattering (SAXS) profiles.

The peak positions in 1D SAXS profiles at higher (Figure 3A) and lower (Figure 3C) temperatures are indexed into μ and ϕ phase, respectively (see Methods). For μ phase, the 20 observed Bragg peaks (Table S7) are indexed according to the *R*-3*m* space group and lattice parameters: $a = b =$ 6.992 nm, c = 39.55 nm. The averaged deviation between observed q values (q_{obs}) and calculated q values (q_{calc}) is 0.037%. For ϕ phase, the 44 observed Bragg peaks (Table S8) are indexed according to the *Imm*2 space group and lattice parameters: a = 6.946 nm, b = 19.011 nm, c = 18.312 nm. The averaged deviation between observed q values (q_{obs}) and calculated q values (q_{calc}) is 0.113%. To better illustrate the agreement between the observed and calculated q values, the theoretical peak positions have been included as drop lines in the experimental SAXS profiles (Figure S17).

2.1.2. Characteristic textures under bright-field transmission electron microscope (BF-TEM).

To better illustrate the characteristics of lattice structure in crystallographic symmetry, we display the textures along multiple orthogonal directions in the main text (Figures 3B, and 3D-G). For μ phase, we captured the textures being tallied with (110) and (001) planes. The corresponding simulated textures are illustrated in Figure S11a, b. For the ϕ phase, we experimentally captured the textures of the (100), (010), and (001) planes. The corresponding simulated textures are illustrated in Figure S11c-e. In BF-TEM, regions with high electron density will appear as dark regions in the resulting image. Given the current molecular structures, aromatic cores are expected to have higher electron density. As a result, the center of each mesoatom should appear as a dark spot in BF-TEM images. Based on each inset (iv) in Figure S11, the proposed positions of spheres correspond well with the dark regions observed in TEM images.

Additionally, FFT images (see Methods) derived from TEM images would serve a good reference to reveal characteristics of lattice symmetry. For comparison, we also simulated electron diffraction patterns of the phase of interest with CrystalMaker (see Methods). As representative, the simulated ED pattern is along the [110] direction for μ phase and long the [100] direction for ϕ phase. Clearly revealed in comparison, strong diffractions of (0 -2 10), (0 0 12), (0 2 11), (0 4 4), (0 4 1), (0 4 -2), and (0 4 -5) along the [110] zone axis (Figure S3a) are correctly reproduced in the μ phase. For the ϕ phase, strong diffractions of (060), (053), (035), and (006) along [100] zone axis (Figure S3b) are also correctly reflected.

2.1.3. Lattice transition between μ and ϕ phases.

The structures of μ and ϕ phases are closely related. In-situ SAXS of molecular pentagon (MP) molecules revealed, in both heating (Figure S4a) and cooling (Figure S4b) processes, the two phases are interchangeable: upon heating (from 150 °C to 210 °C), we observed a ϕ -> μ -> amorphous state phase sequence; upon cooling (from 210 °C to 150 °C), we observed an amorphous state -> μ -> ϕ phase sequence. The enantiotropic phase behavior observed in our

experiments indicates that, within the timeframe of our observations, the μ phase is the stable state at high temperatures, while the ϕ phase is the stable state at low temperatures.

Therefore, by annealing **MP** molecules at an intermediate temperature (190 °C), an intermediate state between μ phase and ϕ phase is anticipated. As revealed in Figure S5, we observed regions of μ phase (region i, (110) plane of μ phase) and ϕ phase (region iii, (100) plane of ϕ phase) intermediated by a transitional state (region ii). The texture of region ii indicates: to transform the (110) plane of μ phase to (100) plane of ϕ phase, an edge dislocation along the slip plane (1-11) of μ phase should occur. Based on this observation, we could derive a unit cell of ϕ phase from its parent structure (μ phase) whose lattice has been extensively studied in metallurgy.

2.1.4. Unit cell reconstruction and simulation of diffraction intensity.

For mesoscale superlattices, accurately simulating powder diffraction patterns (including information such as peak positions, intensities, and broadening) using conventional crystal diffraction software (e.g., CrystalMaker, VESTA, and Material Studio) can be challenging. This is because, although peak positions can be readily confirmed by lattice symmetry, insufficient information about micellar geometry and electron density profile renders accurate reconstruction of scattering intensity almost impossible.

In the present study, we qualitatively simulate the scattering intensity. Micellar superlattices are essentially aromatic cores (central part of molecules) periodically distributed in a continuous matrix consisting of octyl POSS (peripheral part of molecules).[11] The difference of electron density in core and matrix contribute to the scattering intensity. Therefore, to simulate the diffraction intensity, we constructed an atomic cluster (consisting of hundreds of atoms) to mimic the size and geometry of the aromatic core of mesoatom, then place the atomic cluster at the corresponding Wyckoff positions in a lattice with the same dimension of the experimentally determined ones (reconstructed structures are presented in https://doi.org/10.6084/m9.figshare.23497661.v1).

With this reconstructed lattice, we simulated the powder X-ray diffraction (see Methods). These results were further refined incorporating the peak broadening finally resulting in simulated SAXS result in Figure S18. Clearly revealed, the simulated powder diffraction profile qualitatively replicates the strong/weak diffraction peaks as well as the strongly scattered q ranges (q = 0.175–0.225, 0.310–0.340 $Å^{-1}$) in experimentally data (Figures S18a(i) and S16b(i)).

2.1.5. Characterization of cryo-microtomed samples

The thin-film sample characterized under TEM is prepared by drop-casting (see Methods). We did not prepare samples by microtoming because of samples' low glass transition temperature (~10 °C, Figure S2). Inevitable lattice deformation during microtoming also add to the challenge in structural determination.

Nevertheless, to rule out the influence of sample preparation during structural formation, we also annealed the bulk sample (the same method for samples in SAXS characterization) then prepared a thin-film sample by cryo-microtoming (see Methods). By doing so, we successfully captured the identical (100), (010), and (001) planes of ϕ phase (Figure S19). This result suggests that thin-film sample would have the identical self-assembled structures with that in bulk state.

2.2. Quantities of molecules per mesoatom and size distribution of mesoatoms

The size of a mesoatom is determined by the quantity of molecules per mesoatom. To characterize averaged sizes of mesoatoms, qualitatively, one could calculate an averaged number of molecules in one mesoatom ($\bar{N}$) globally. One could also estimate size distribution based on the volume of

Wigner–Seitz (WS) cells, or estimate the combination of molecular number (N) at each Wyckoff site that constitutes $\bar{N}$ values.

The averaged number of molecules in one mesoatom ($\bar{N}$) is defined as $\bar{N} = \frac{V_c}{nV_m}$, where n is the number of mesoatoms in a unit cell, V_c and V_m are the volume of unit cell and molecule, respectively. The V_c is expressed as a^3 for the cubic lattices (BCC-type phases), abc for the orthorhombic phase (ϕ phase), or $\frac{\sqrt{3}}{2}a^2c$ for the trigonal phase (μ phase), where a, b, and c are lattice parameters determined by SAXS. The V_m is estimated by $\frac{M_m}{N_A\rho}$, where M_m is the relative molecular mass, ρ is the density of material, and N_A is the Avogadro constant. The $\bar{N}$ values for all phases in the present study are summarized in Table S9.

In a crystal lattice, a WS cell of an atom consists of all points in space that are closer to that central atom than to any other.[12] Mathematically, a WS cell can be regarded as the region enclosed by the boundaries defined by the perpendicular bisectors of all line segments connecting the central atom to its neighboring atoms. In other word, a WS cell reflects the space that is potentially occupied by a central atom. However, it is important to note that the WS cell is just an indicator of micellar geometry in a dense packing state rather than an accurate evaluation of micellar volume. In reality, neighboring atoms may have different volumes, which renders the segmentation based on perpendicular bisector planes invalid. Therefore, we only use the WS cell as a qualitative illustration of size distribution, as shown in Figure S9.

One could also qualitatively estimate the molecular number (N) at each Wyckoff site based on the overall $\bar{N}$ values. Since the molecular number in each mesoatom (N) should be an integer, the fractional $\bar{N}$ values indicate the variance of N at different Wyckoff sites in lattice. For example, BCC-type phase formed by **M2** is determined to be $\bar{N} = 4.10$ (Table S9), which suggests all sites in this structure should be occupied by 4-molecule mesoatoms. In another case, for example, BCC-type phase formed by **M1**, the fractional $\bar{N} = 6.56$ indicates mesoatoms in two different sizes (6-molecule and 7-molecule) coexist in one lattice. When the types of Wyckoff sites increased to 5 and 14, as in μ and ϕ phase respectively, the combinations of N becomes significantly more complicated. In Table S10, we list the most probable combinations of N. The combinations are postulated based on three criteria: 1. The calculated $\bar{N}_{calc} = \frac{\sum_1^n N_n}{n}$ should be close to the experimental $\bar{N}$ values (Table S10). 2. The calculated aspect ratios R based on the geometry of WS cells (Figure 5C) should be close the simulated R of mesoatoms with different molecules (Figure S10); 3. The simulated diffraction profile of lattice with the combination of N (see Methods) should well reflect the features in experimental profiles (Figure S18). Based on these criteria, for the 39 mesoatoms in a lattice of μ phase, the optimal numbers of 3-, 4-, and 5-molecule mesoatoms are 27, 6, and 6 (with a ratio of 9:2:2). For the 54 mesoatoms in a lattice of ϕ phase, the optimal numbers of 3-, 4-, 5-, and 6-molecule mesoatoms are 32, 12, 8, and 2 (with a ratio of 16:6:4:1).

2.3. Stability of ϕ phase

To gain deeper insights into the factors contributing to the broad distribution of mesoatoms in **MP**, molecular dynamics simulations were conducted (see Supplementary Information 1.3). We first evaluate the energy of molecules by placing mesoatoms with different molecular numbers (*i.e.*, *N* = 3, 4, 5, or 6) in a lattice of ϕ phase (Figure S15). It is surprising that only the five-fold **MP** exhibits almost equal energies in all four types of mesoatoms. Therefore, the near-equal energy suggests, in terms of enthalpy, the driving force for **MP** to unify mesoatomic sizes would be

minimal. In contrast, other molecules tend to have one dominant size (Figure S15), which enthalpically destabilizes the ϕ phase, driving the system into a lattice with uniform mesoatoms, such as in BCC-type lattice. By placing molecules in BCC-type lattices, we also calculate the enthalpy of molecules in mesoatoms with different molecular numbers (*i.e.*, N = 3, 4, 5, or 6). We observed N with low energy tally well with experimentally observed molecular numbers (Figure S16a).

We then compare the energetics between BCC and ϕ phase. Specifically, for molecules **M1** to **M4**, it is found that some mesoatoms in the ϕ phase exhibit lower local energy than their counterparts in the BCC phase. For instance, the local energy of **M2** with a cluster size of 5 molecules is -66.2 kJ/mol (Figure S15), which is lower than the local energy of clusters of different sizes in the BCC phases (Figure S16a). However, it is crucial to note that clusters with high local energy are also present concurrently in the ϕ phase. For example, the local energy of **M2** cluster with a size of 6 is -19.4 kJ/mol. This inherent variability inevitably leads to a higher average cluster energy in the ϕ phase (Figure S16b), which is unfavorable for the formation of the ϕ phase but conducive to the formation of the BCC phase. In the case of **MP** molecules, our findings suggest that the BCC phase has a higher energy level compared to the ϕ phase (as depicted in Figure S16b) when we estimate the number of molecules in mesoatoms (N = 3 and 4) based on the experimental results of **M3**, whose chemical structure closely resembles that of **MP**. Nevertheless, our simulations also reveal that clusters of size 5 within the BCC phase exhibit a lower cluster interaction energy in comparison to the ϕ phase for **MP**. This intriguing observation implies that entropic contributions play a pivotal role in promoting the formation of the ϕ phase.

While it is challenging to precisely quantify the entropic contributions, we can conceptually categorize entropy based on the scale of its contributing degrees of freedom. In other words, entropy can be delineated into three primary domains: packing free volume, cluster size distribution, and molecular conformation.

2.3.1. Entropy associated with free volume.

Our system exemplifies a soft matter assembly paradigm, inherently capable of adaptive reshaping to optimize spatial occupancy. This leads us to anticipate that entropy contributions stemming from free volume are inconsequential. It's important to note that this concept differs significantly from the entropy dynamics observed in hard colloid assemblies, where such factors play a significant role.[12,13]

2.3.2. Entropy associated with cluster distribution.

To gauge the entropy concerning cluster distribution, we employed the Gibbs entropy formula

$$S = -k \sum_i p_i \ln p_i$$

Wherein, S denotes the entropy per molecule linked to the distribution of mimesoatos of varied sizes, k stands for the Boltzmann constant, and p_i is the probability of encountering a specific molecule within a mesoatom comprising *i* molecules.

Considering BCC crystals, the mesoatom distribution is monodispersed, leading to $p_i = 1$ for a given *i* and 0 for the remaining *i* values. This results in $S = 0$ for the BCC crystal structure when molecular number is monodispersed. For the ϕ phase, the size distribution of mesoatoms can be derived from the experimentally determined crystal cell (Supplementary Information 2.2). The ensuing entropy computation yields $S = 1.189k$, or 9.890 J/mol/K (Table S11). When assessed at 180°C (equivalent to 453K), the free energy contribution owing to this entropy element is $-T\Delta S = -4.48$ kJ/mol. Though this value remains notably lower than the energy differentials

observed for individual molecules, the entropy caused by the broaden size distribution promote the formation ϕ phase.

2.3.3. Entropy associated with molecular conformation.

Due to non-rigid alkyl chains on POSS cages, the overall shape of mesoatom could deform by change of chain conformation. In the transition from BCC to ϕ phase, the local packing environment of mesoatoms varies, leading to changes in the stretchiness of alkyl chains on POSS cages. In conventional systems packed by soft chain-like molecules, a spherical geometry is typically favored[14] to maximizing the achievable chain conformation while minimizing the interfacial area. This is the primary reason for the stability of BCC and some other phases with high sphericity of building blocks. However, in the present semi-rigid system, based on the simulation of conformation of mesoatoms, the unconfined geometry may largely deviate from a sphere (Figure 5D), which mean BCC lattice may induce additional stretchiness to alkyl groups. Therefore, the lattice which highly deformed WS cell (like the ϕ phase) is also favorable in terms of entropy associated with molecular conformation.

In summary, with regard to entropy, the complex ϕ phase is favored over the BCC phase for all molecules involved (**MP** and **M1-4**). However, concerning enthalpy, only **MP** exhibits nearly equal energy levels across all molecular numbers. For **M1-4**, a dominant molecular number with low energy drives the system toward uniform-sized mesoatoms, ultimately resulting in conventional spherical packing structures.

2.4. The absence of ϕ phase in metal alloys

In rationalizing the Hume-Rothery rule (*i.e.*, binary alloys' phase dependence on the concentration of valence electrons), people anticipate metallic alloys would favor a crystal structure whose free-electron-like Fermi surface (presumably being spherical) would be mostly enclosed by the Jones zone.[15] This concept has also been adopted by polymeric systems to account for the stability of high-sphericity phases.[13]

The rationalization would help us to understand why the ϕ phase is absent in metal alloys. In practice, we simulated the powder diffraction of A15, σ, μ and ϕ phases with Cu atoms. Then we adopted the strong diffractions to reconstruct the Jones zone in reciprocal space (see Methods) and evaluate its geometric features. The shape of Jones zones of A15, σ, μ and ϕ phases are illustrated in Figure S14. Since Jones zones are convex polyhedra, to evaluate its deformation from perfect sphere, we also applied the method described in Methods to afford R (Table S5). Clearly, the ϕ phase is with a rather high R value, suggesting the Fermi sphere would be less effectively enclosed (*i.e.*, The Fermi sphere would touch the Jones Zone along the direction of the short axis, while leaving a greater distance to the boundary of the Jones Zone along the long axis). Therefore, the ϕ phase would be less stable in free-electron-like systems.

3. Supplementary Figures

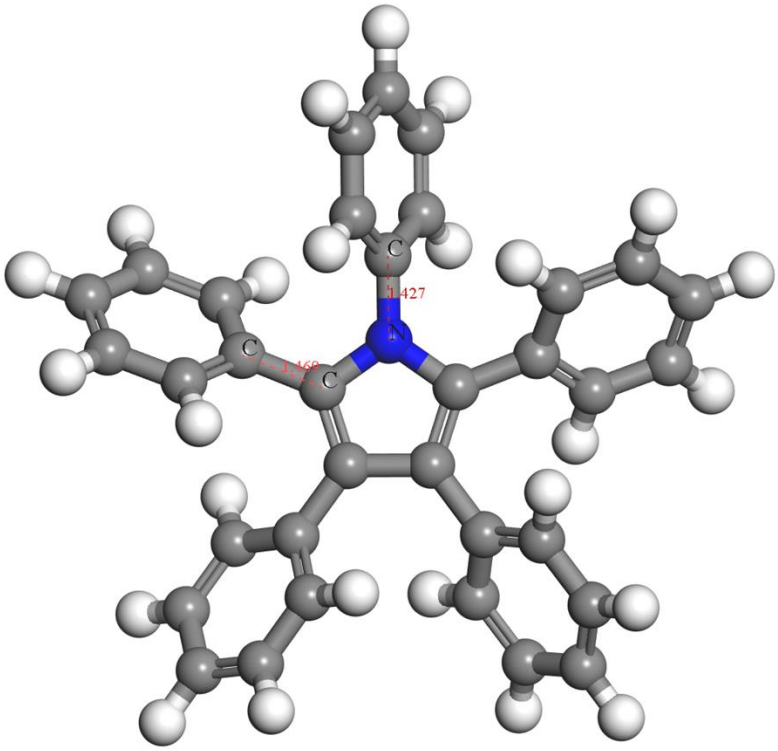

Figure S1. Optimized geometry of pentaphenyl pyrrole. The length of C-C bonds is 0.0042 nm longer than that of C-N bond (0.1469 nm for a C-C bond and 0.1427 nm for a C-N bond). we anticipate the 0.0042 nm fluctuation in bond length is largely compensated in **MP** by fuzzy POSS cages (~ 1.3 nm in diameter). Method of geometric optimization is presented in Methods.

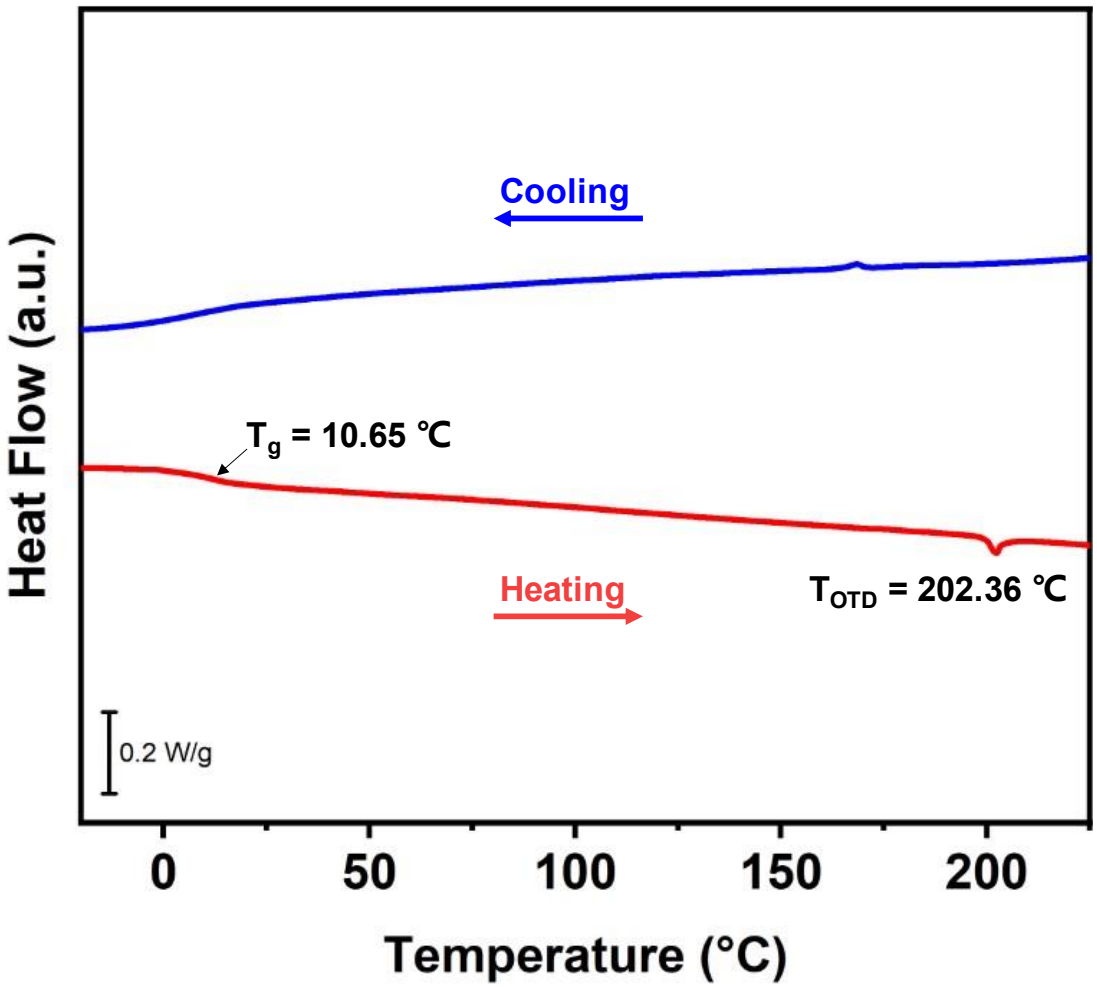

Figure S2. The DSC thermograms of MP. The data were obtained during the first cooling and second heating at 10 ℃/min.

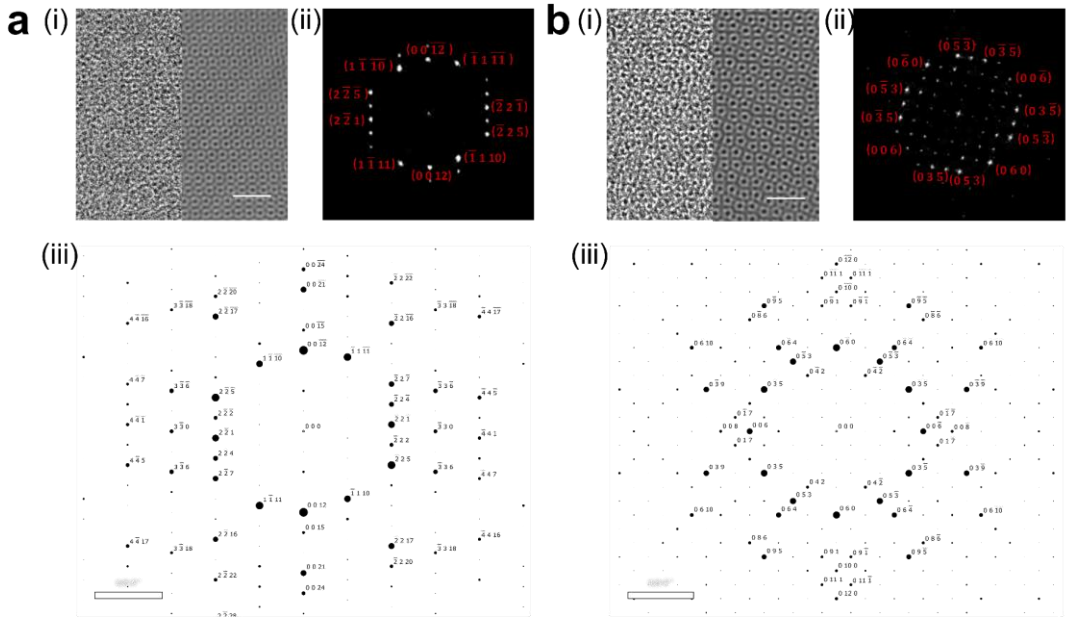

Figure S3. Experimental TEM results ((i) TEM image in real space, (ii) FFT image in reciprocal space) and (iii) simulated weighted reciprocal lattice of (a) (110) plane μ phase. (b) (100) plane of ϕ phase. Scale bar: 20 nm.

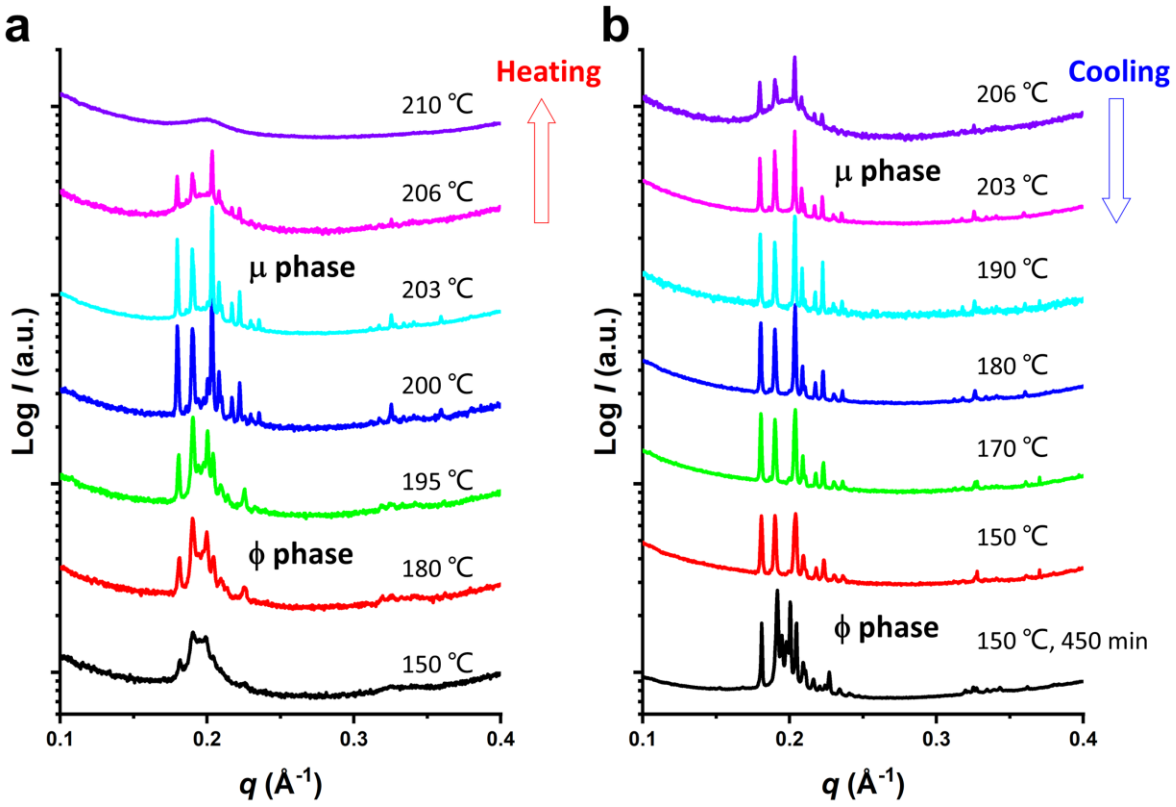

Figure S4. In-situ SAXS characterization of **MP** molecule with smaller temperature intervals compared to those shown in Figures 3H and 3I. (a) Heating process. (b) Cooling process.

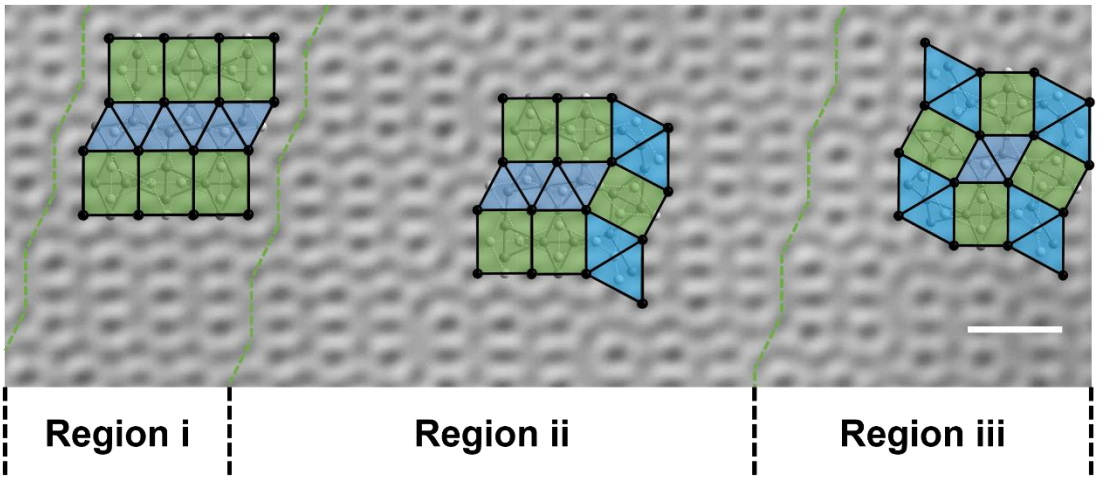

Figure S5. Crystal lattice changing from μ phase to ϕ phase. The region i represents a microdomain of μ phase; the region ii represents a microdomain of an intermediate phase; the region iii represents a microdomain of ϕ phase. Scale bar: 20 nm

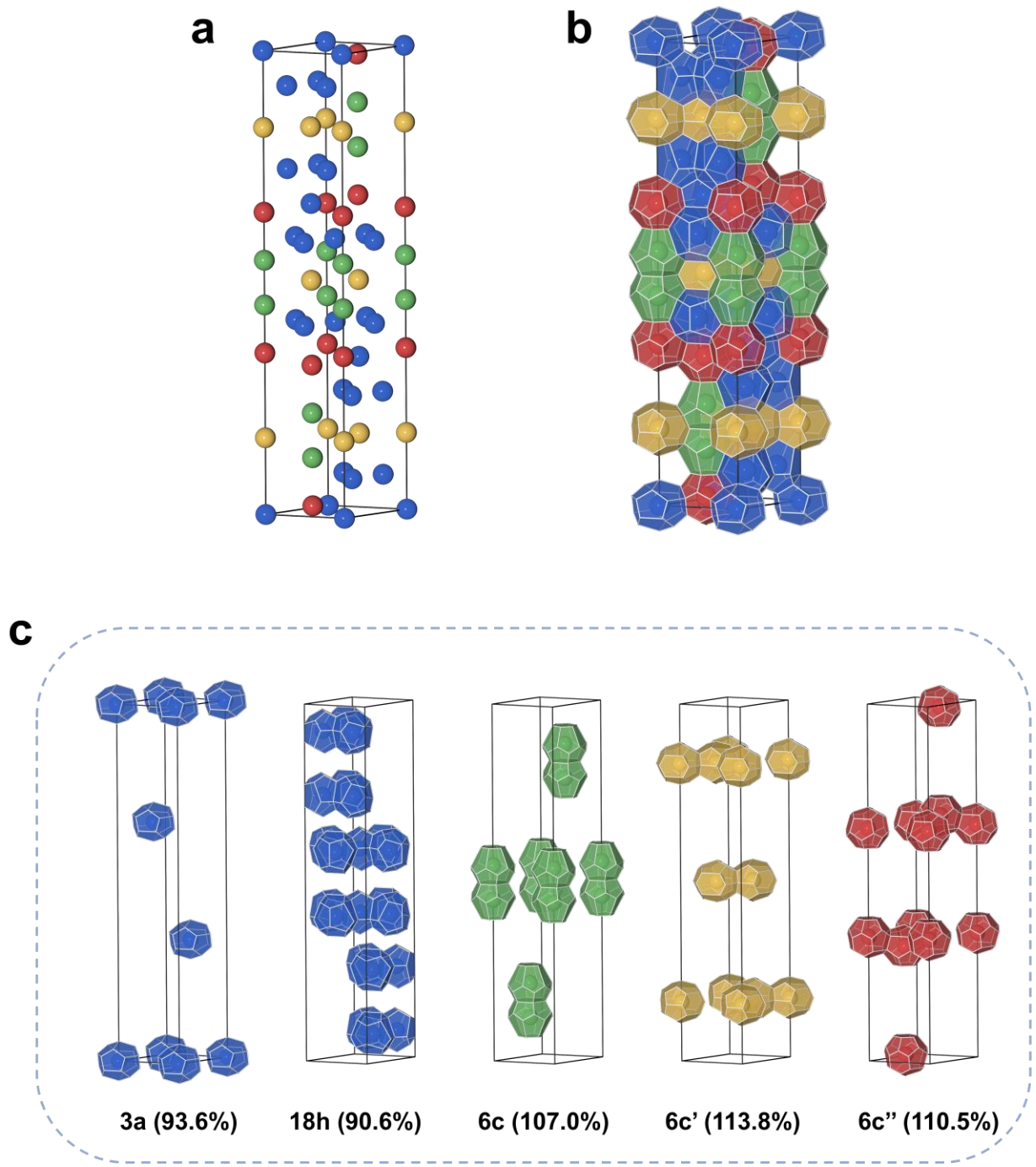

Figure S6. (a) μ phase unit cell with all the five different types of particles. (b) Space-filling representation depicting Wigner-Seitz (WS) cells surrounding the particles. (c) show the WS cells surrounding the particles for particles with Wyckoff positions 3a, 18h, 6c, 6c' and 6c'', respectively. The percentages given in (c) are the relative volumes of the respective WS cell with respect to the number average volume of the all the five types of WS cells. All color codes follow the ones in Figure 1A (blue, green, yellow, and red colors stand for 12-, 14-, 15-, and 16-coordinating environment, respectively).

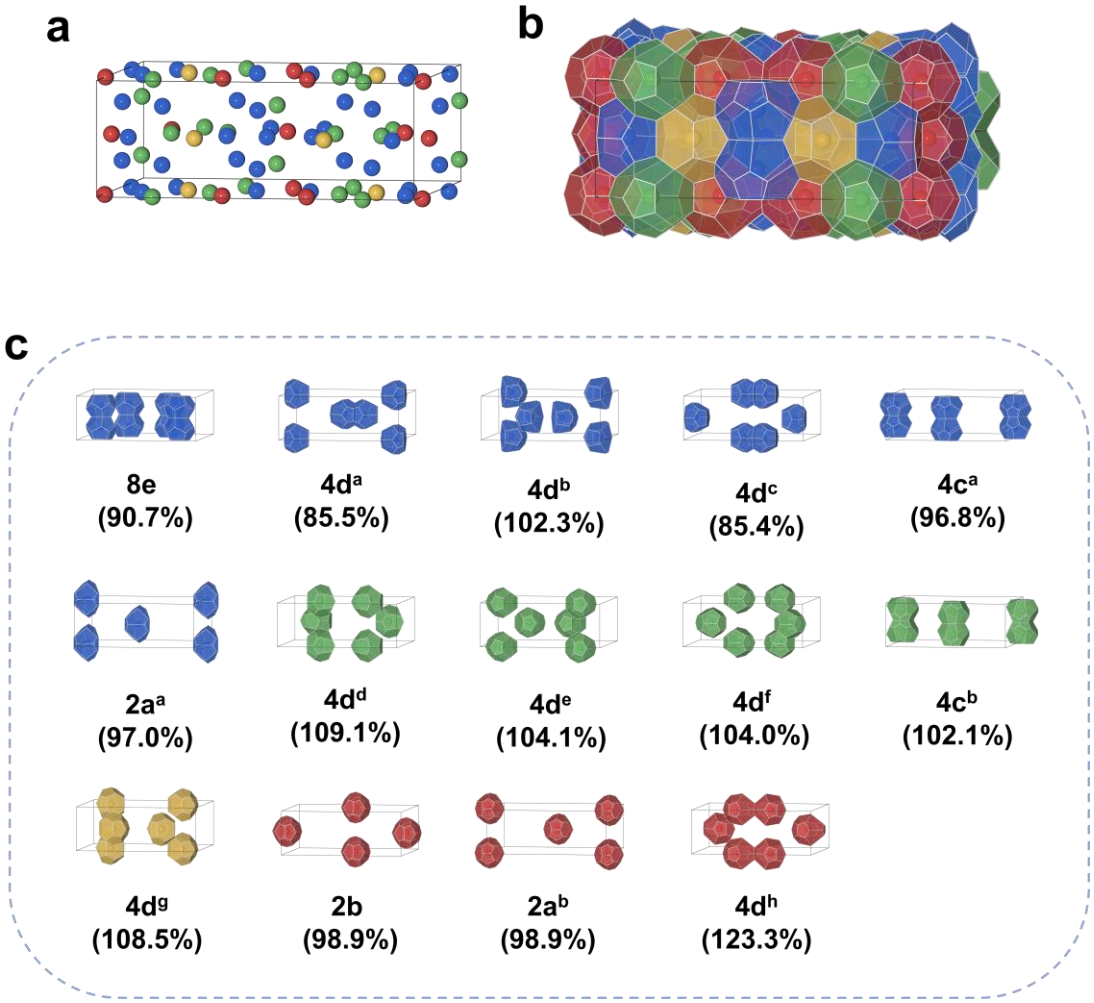

Figure S7. (a) ϕ phase unit cell with all the 14 different types of particles. (b) Space-filling representation depicting Wigner-Seitz (WS) cells surrounding the particles. (c) show the WS cells surrounding the particles for particles with different Wyckoff positions. The percentages given in (c) are the relative volumes of the respective WS cell with respect to the number average volume of the all the five types of WS cells. All color codes follow the ones in Figure 1A (blue, green, yellow, and red colors stand for 12-, 14-, 15-, and 16-coordinating environment, respectively).

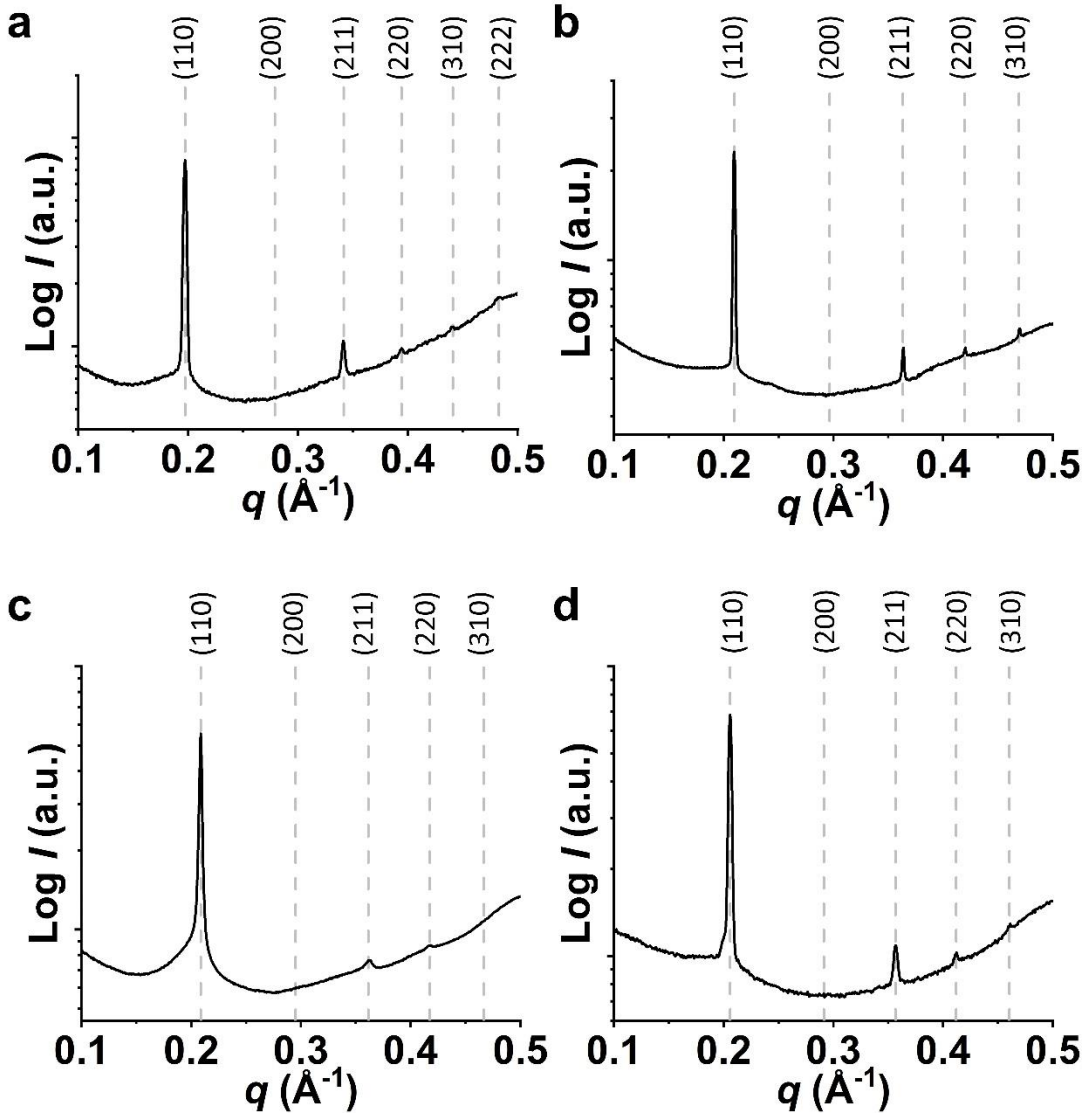

Figure S8. SAXS pattern for the BCC phase based on (a) **M1**, (b) **M2**, (c) **M3**, (d) **M4**.

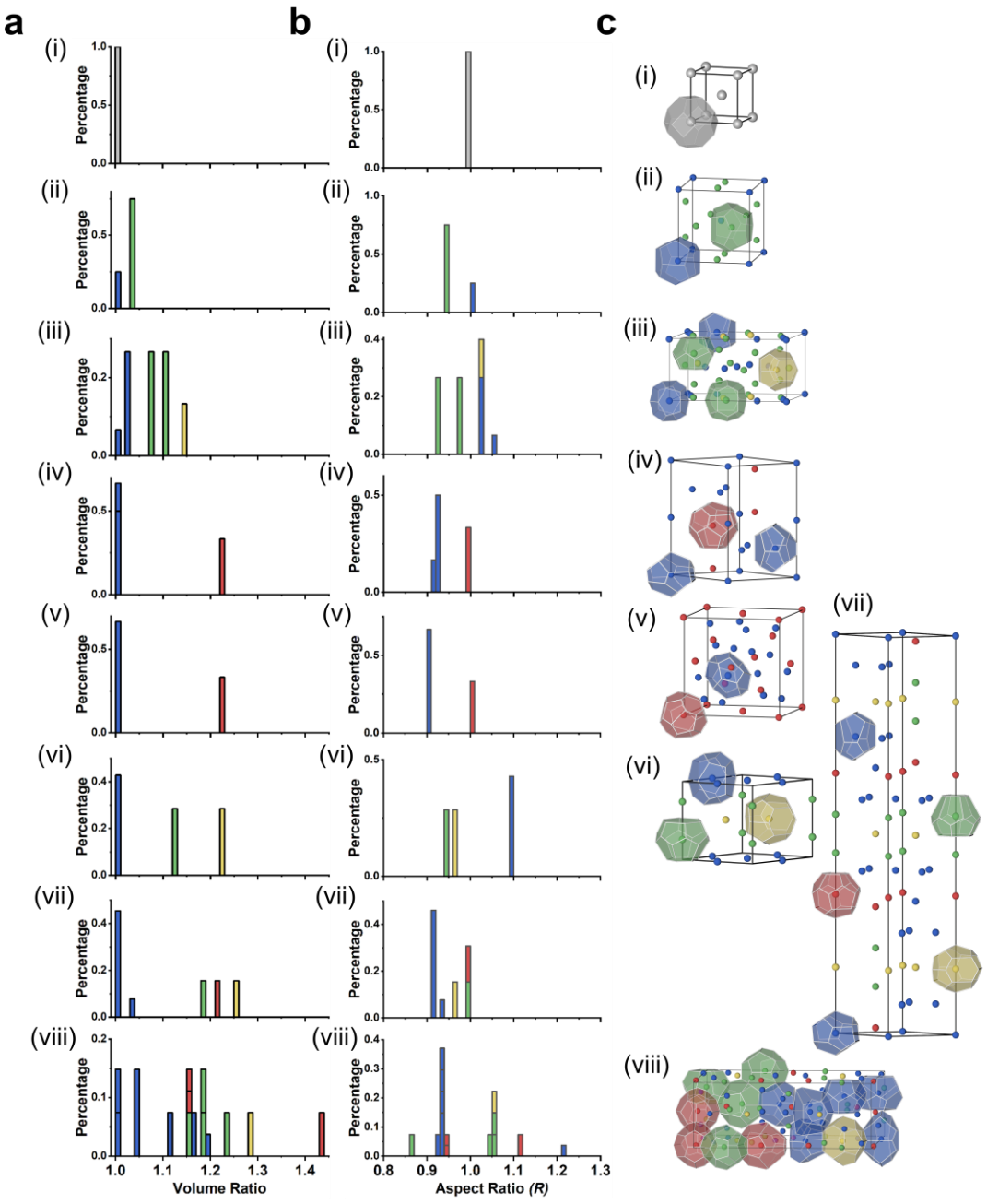

Figure S9. (a) The normalized frequency of volume ratios of all WS cells in (i) BCC phase, (ii) A15 phase, (iii) σ phase, (iv) C14 phase, (v) C15 phase, (vi) Z phase, (vii) μ phase, and (viii) ϕ phase. (b) The normalized frequency of *R* values of all WS cells in (i) BCC phase, (ii) A15 phase, (iii) σ phase, (iv) C14 phase, (v) C15 phase, (vi) Z phase, (vii) μ phase, and (viii) ϕ phase. (c) lattice structure of (i) BCC phase, (ii) A15 phase, (iii) σ phase, (iv) C14 phase, (v) C15 phase, (vi) Z phase, (vii) μ phase, and (viii) ϕ phase. For each Wyckoff position, one WS cell is illustrated as representative. For all FK phases, color codes follow that in Figure 1A.

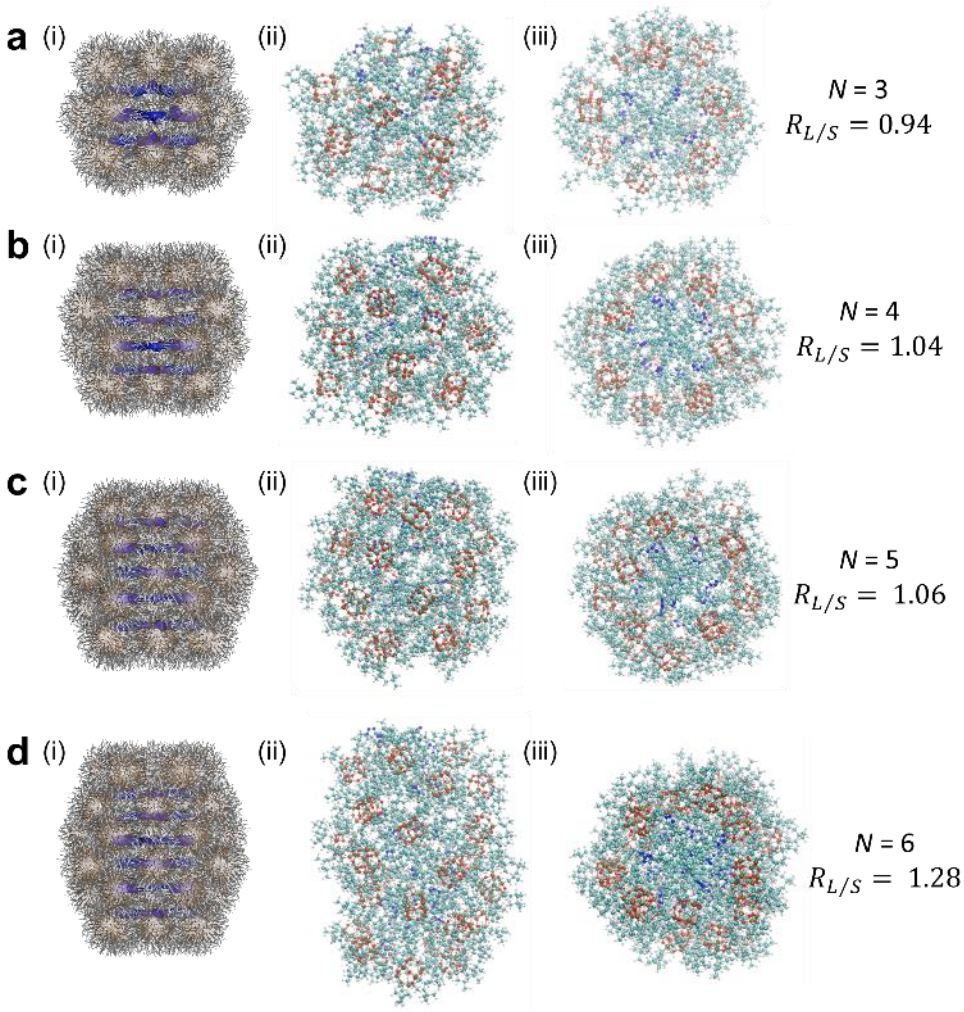

Figure S10. Deformation of uniaxial stacked mesoatoms with molecular number (***N***). (a) ***N*** = 3, (b) ***N*** = 4, (c) ***N*** = 5, and (d) ***N*** = 6. In each panel, inset (i) is a model of uniaxial stacking of ***N*** disc-like molecules; inset (ii) is the side view of simulated conformation of mesoatom; inset (iii) is the top view of simulated conformation of mesoatom. Aspect ratio *R* corresponding to each mesoatom is labeled aside. Simulation method is presented in Methods, method to calculate *R* values is presented in Supplementary Information 1.3.

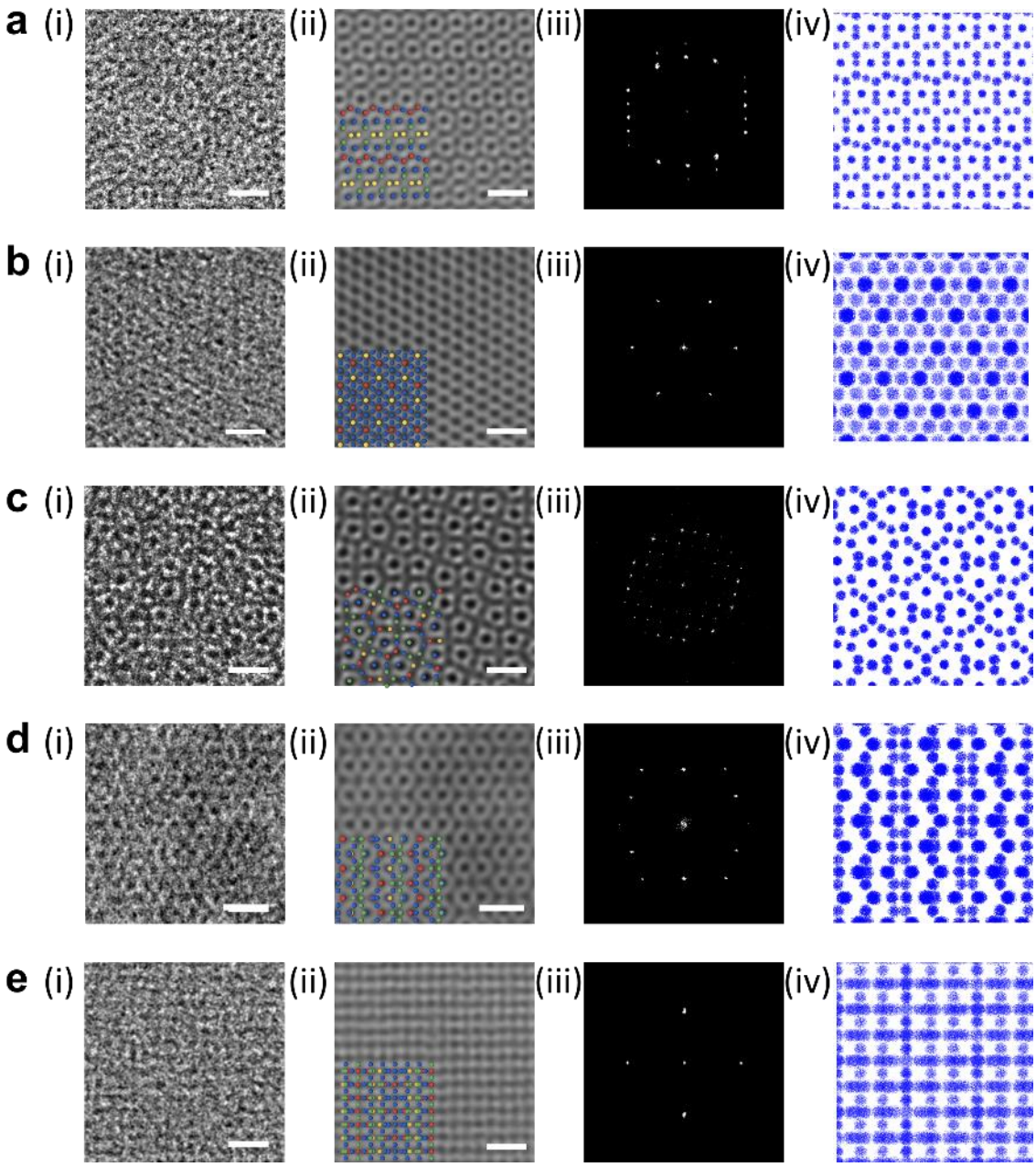

Figure S11. Comparison between experimental BF-TEM images (bottom textures) and simulated textures based on proposed lattice structures (top textures). (a) (110) plane of μ phase, (b) (001) plane of μ phase. (c) (100) plane of ϕ phase. (d) (010) plane of ϕ phase. (e) (001) plane of ϕ phase. For each panel, the inset (i) represents original image, the inset (ii) represents Fourier-filtered image (see Methods), the inset (iii) represents fast Fourier transform (FFT) image, the inset (iv) represents simulated texture (see Methods). Scale bar: 10 nm.

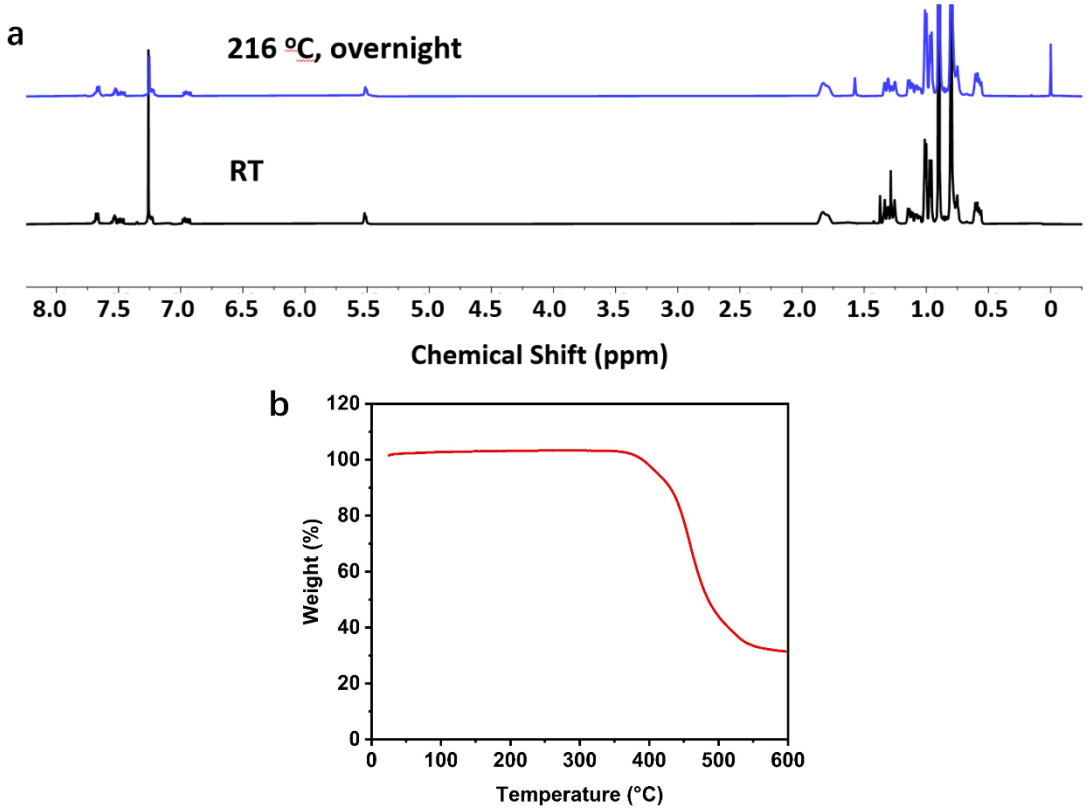

Figure S12. Thermal stability of **MP**. (a) ^{1}H NMR spectrum before (bottom) and after (top) overnight thermal treatment. (b) TGA curve.

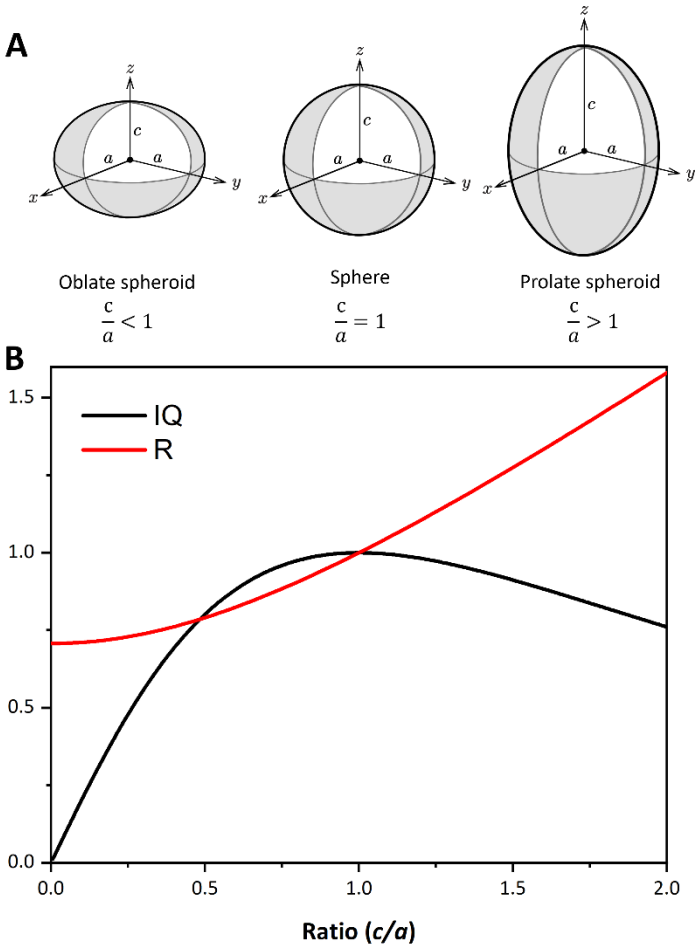

Figure S13. (A) Schematic illustration of the transition from an oblate spheroid ($c < a$) to a prolate spheroid ($c > a$). (B) Graph depicting *IQ* (black line) and *R* (red line) functions. It is evident that the *IQ* value does not distinguish between the oblate and prolate cases.

5

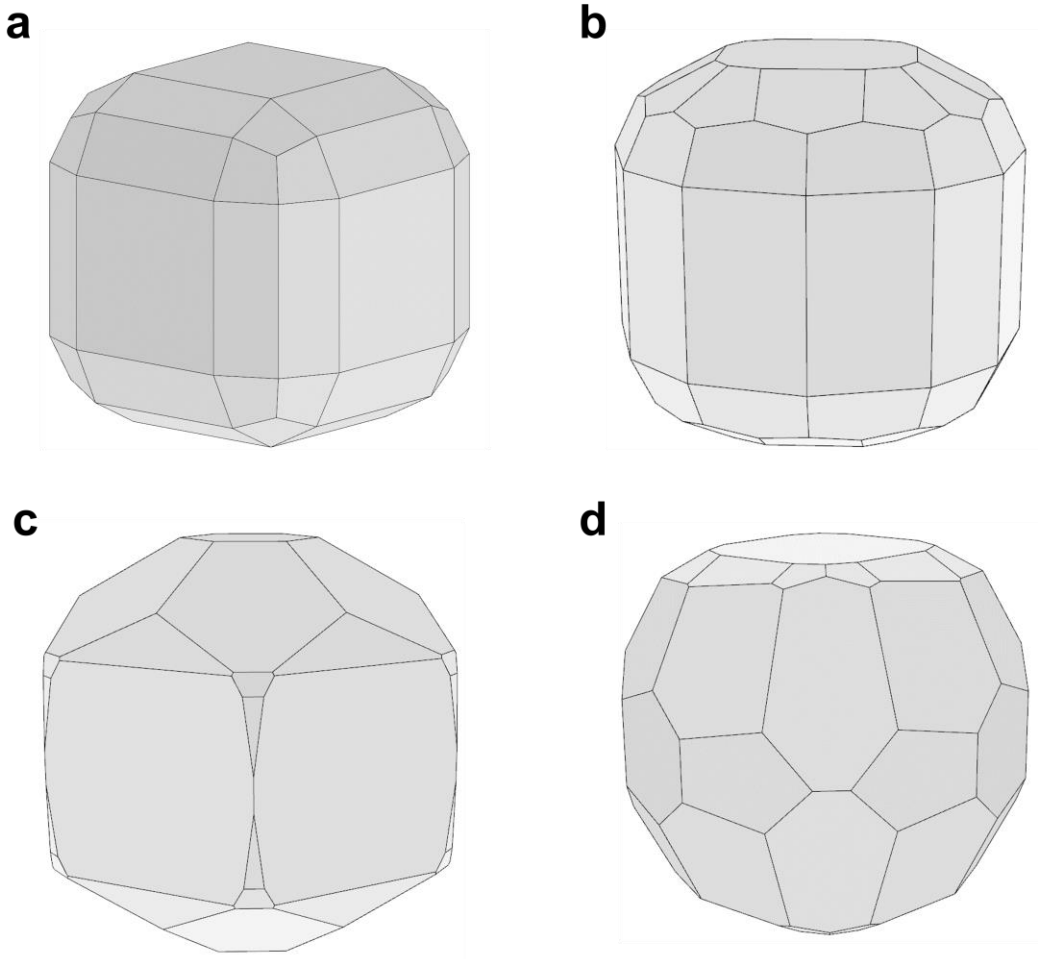

Figure S14. Jones zones of (a) A15, (b) σ, (c) μ and (d) ϕ phases.

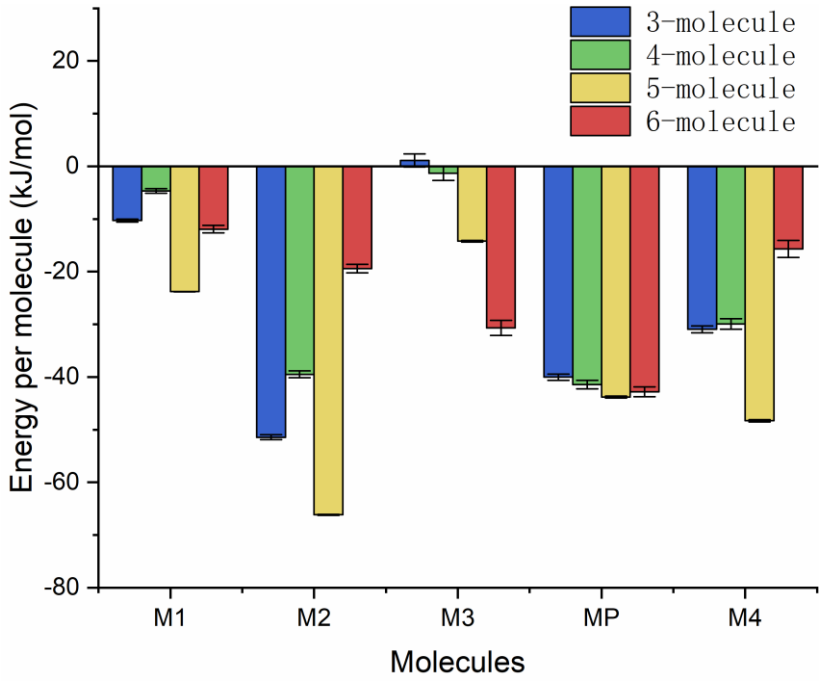

Figure S15. Energy of **MP** and **M1–4** in *N*-molecule mesoatoms in ϕ phase. Error bars represent the standard errors. Data are presented as mean values with standard errors. The average value and standard errors are calculated from 501 snapshots, each separated by 10 ps, extracted from the final 5 ns of molecular dynamics simulations.

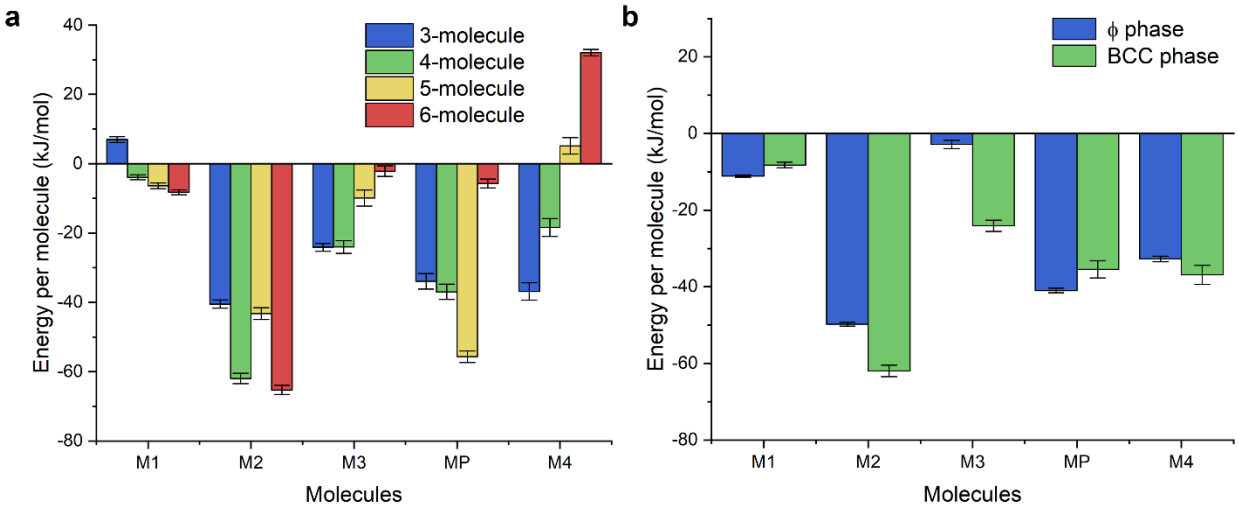

Figure S16. (a) Energy of **MP** and **M1-4** in *N*-molecule mesoatoms in BCC phase. Asterisk denotes the experimental determined most stable *N* values in BCC lattices (Table S9). Simulation method presented in Methods. (b) Energy comparison between ϕ phase and BCC phase. The energetics of experimentally accessible structures (BCC for **M1-4** and ϕ phase for **MP**) are estimated through a weighted averaging process that considers the energetics of experimentally observed combinations of *N*-molecule mesoatoms. In the case of the experimentally inaccessible ϕ phase for **M1-4**, their energetics are estimated by following a similar approach based on the combination of **MP** data. Additionally, for the BCC phase of **MP**, its energy is estimated using experimental data from the combination of **M3**. Data are presented as mean values with standard errors. The average value and standard errors are calculated from 501 snapshots, each separated by 10 ps, extracted from the final 5 ns of molecular dynamics simulations.

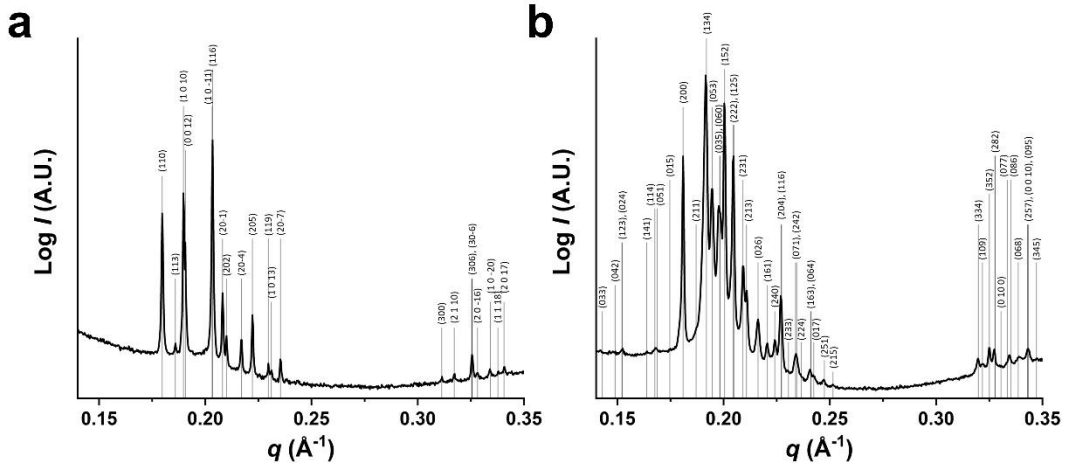

Figure S17. SAXS profiles for (a) μ phase and (b) ϕ phase. Droplines indicate the Miller index of the corresponding Bragg peak. The q values of experimental and simulated Bragg peaks are listed in Table S7 and Table S8, respectively.

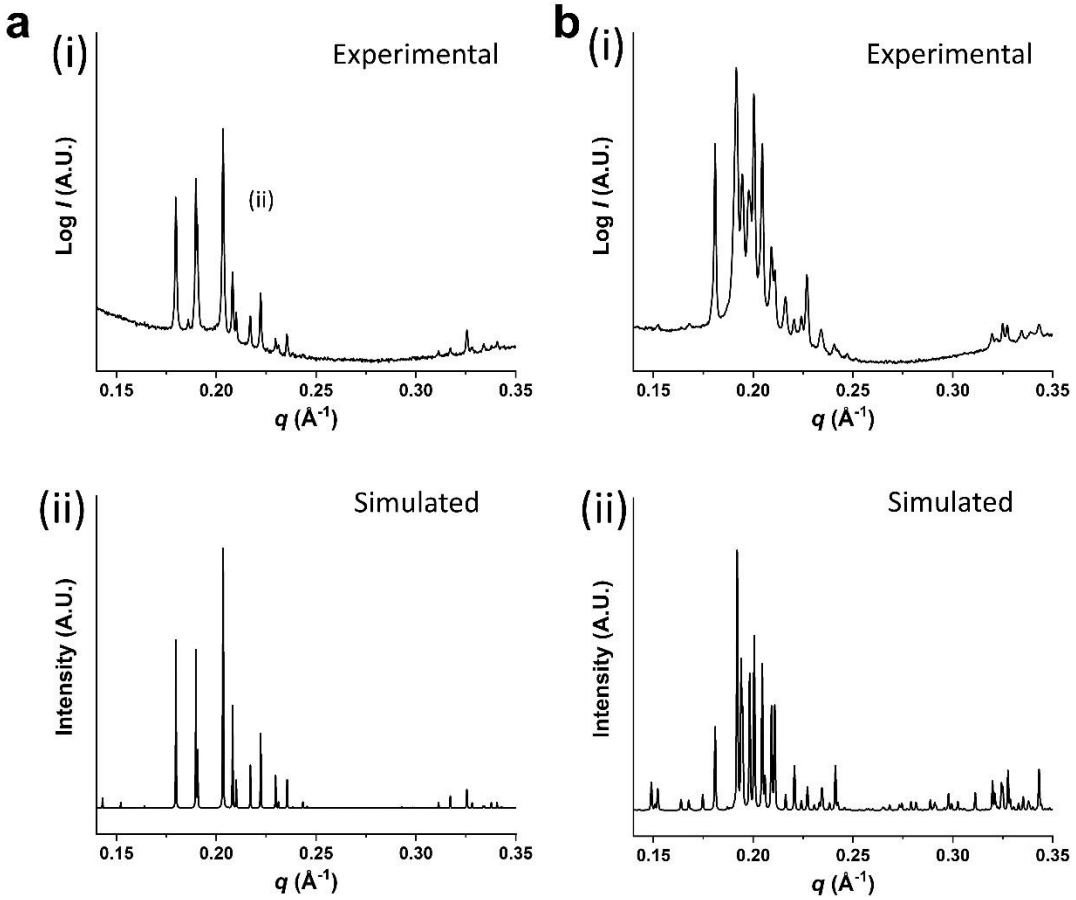

Figure S18. Comparison between experimental SAXS profiles and simulated SAXS profiles based on full-size micellar model. (a) μ phase, (i) experimental data, (ii) simulated data. (b) ϕ phase, (i) experimental data, (ii) simulated data.

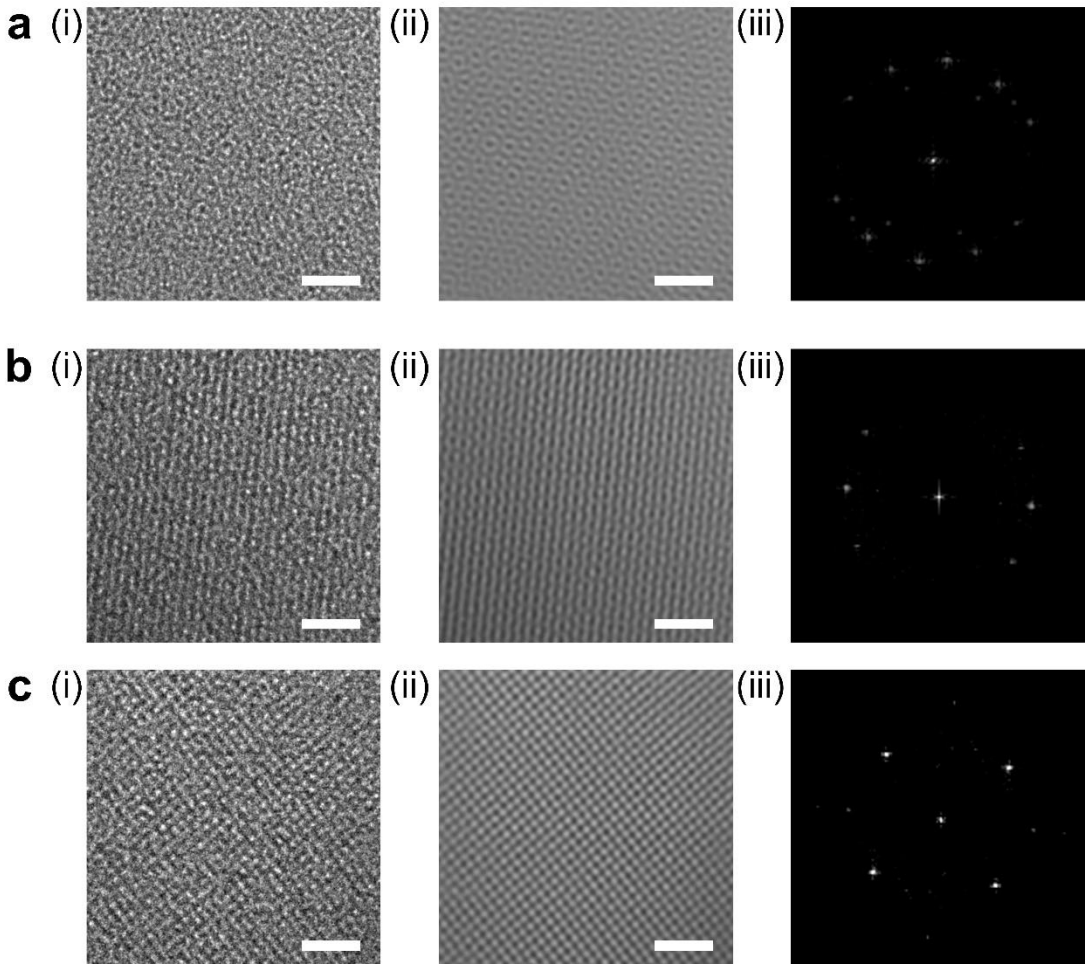

Figure S19. Cryo-microtomed sample with (a) (100) plane, (b) (010) plane, and (c) (001) plane of ϕ phase. For each panel, the inset (i) represents an original TEM image, the inset (ii) represents a Fourier-filtered image (see Methods), and the inset (iii) represents a FFT image (see Methods). Scale bar: 20 nm

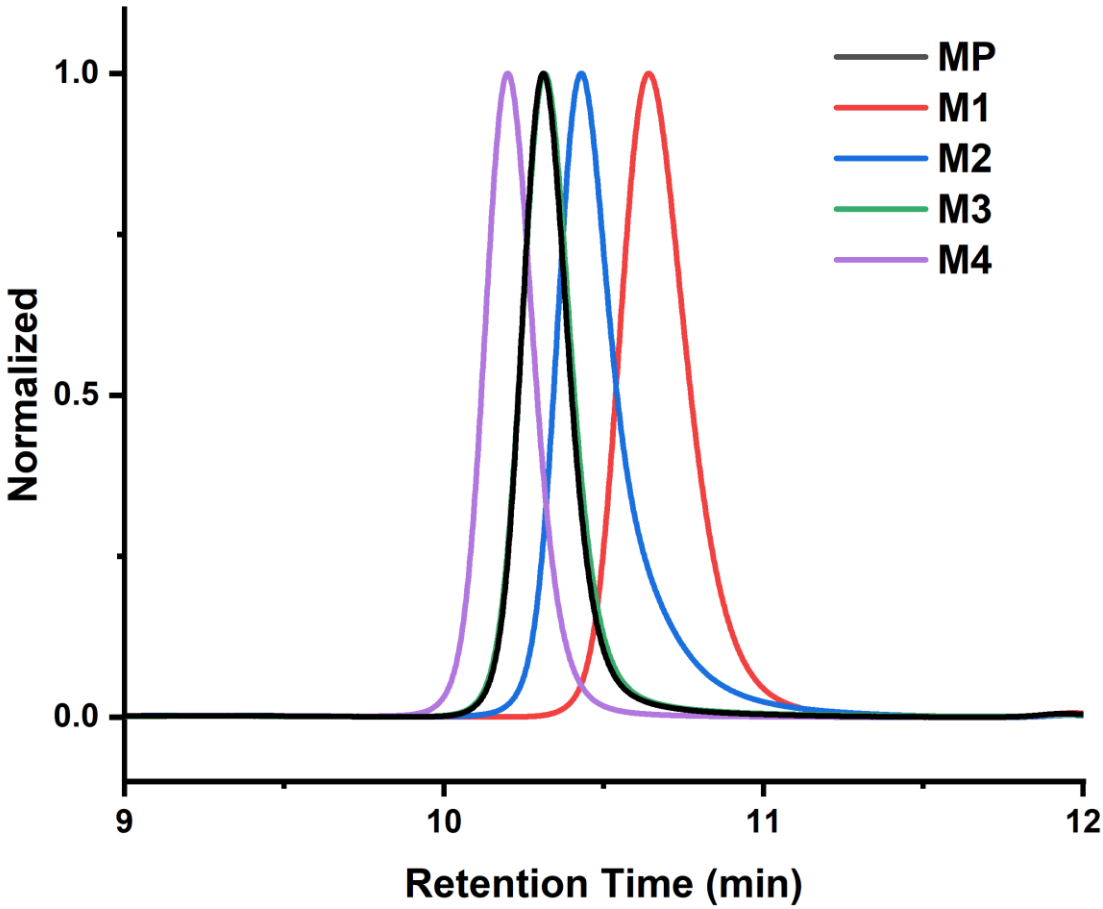

Figure S20. GPC profiles of giant molecules **MP**, **M1**, **M2**, **M3** and **M4**.

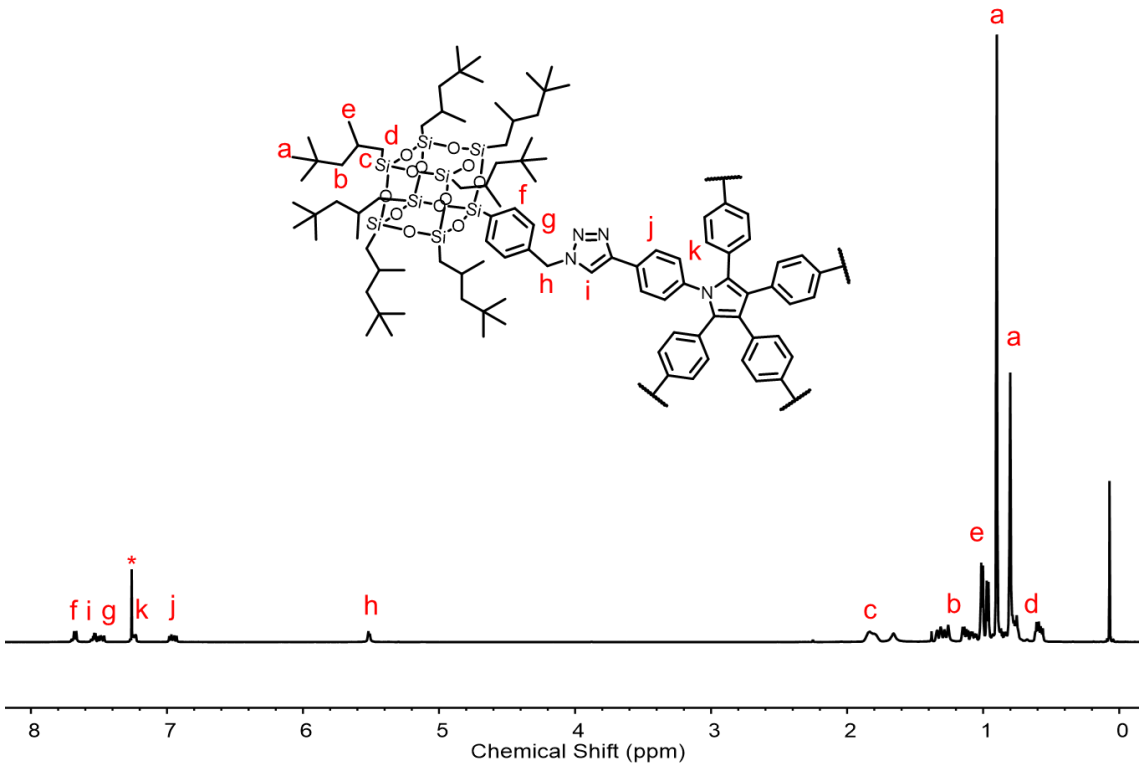

Figure S21. ^{1}H NMR spectra of **MP**.

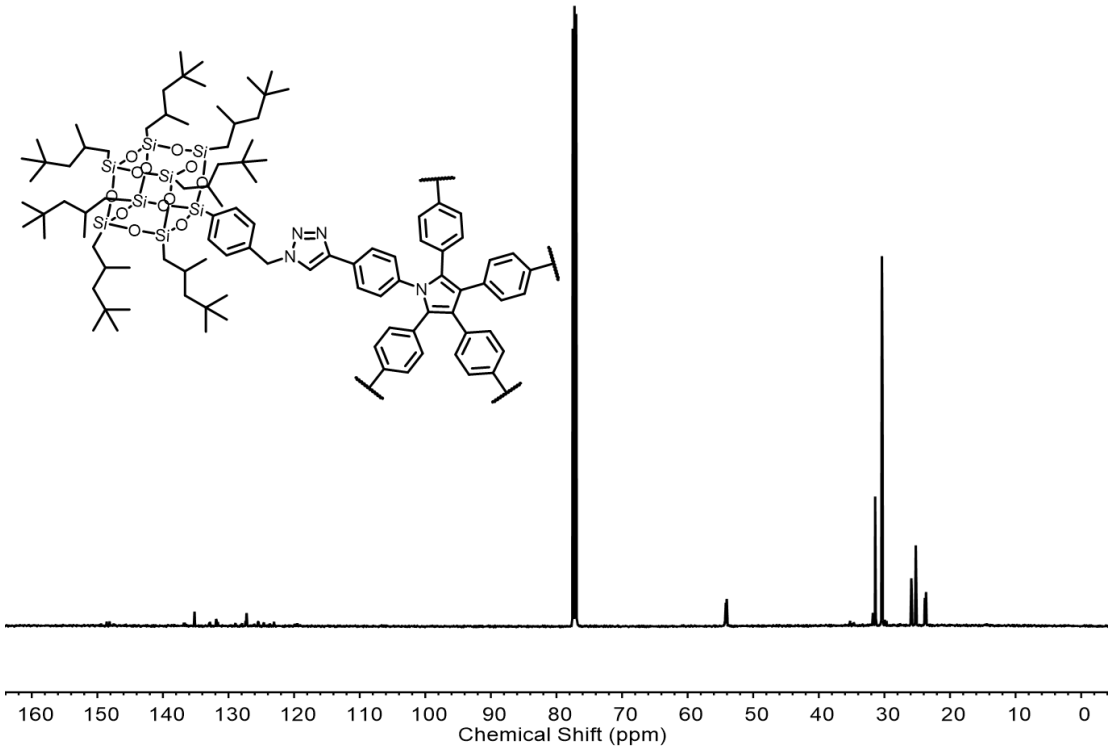

Figure S22. ^{13}C NMR spectra of **MP**.

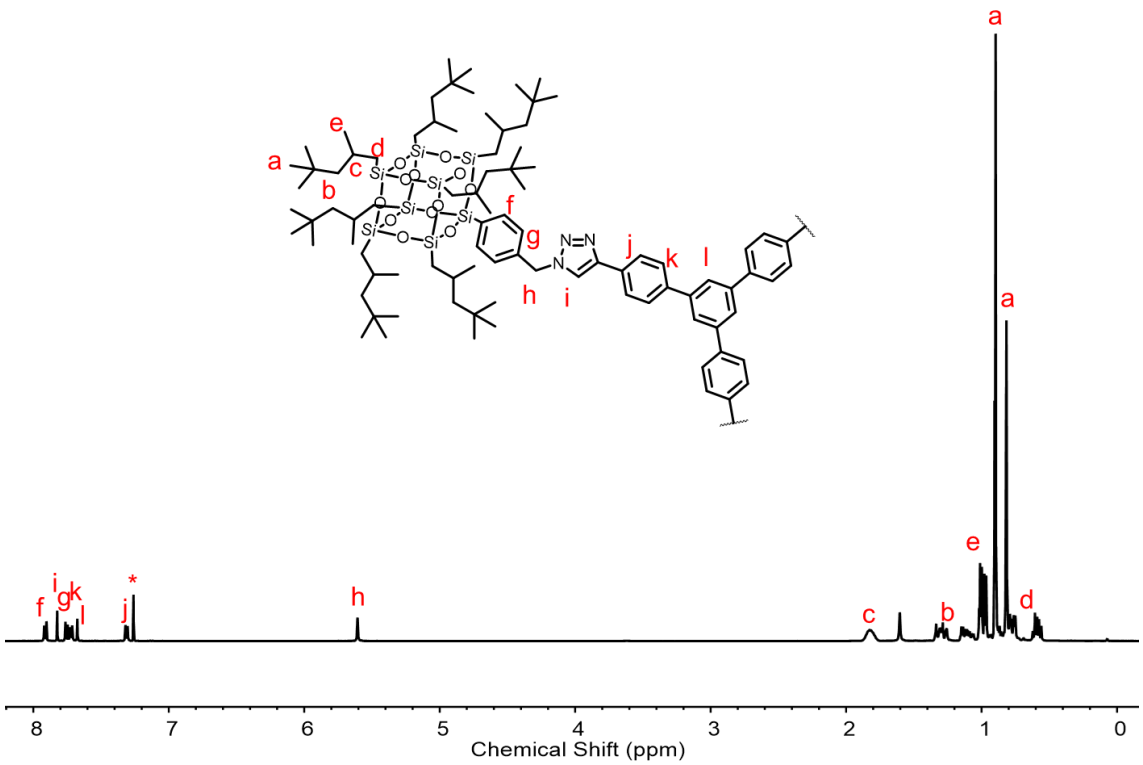

Figure S23. ^{1}H NMR spectra of **M1**.

5

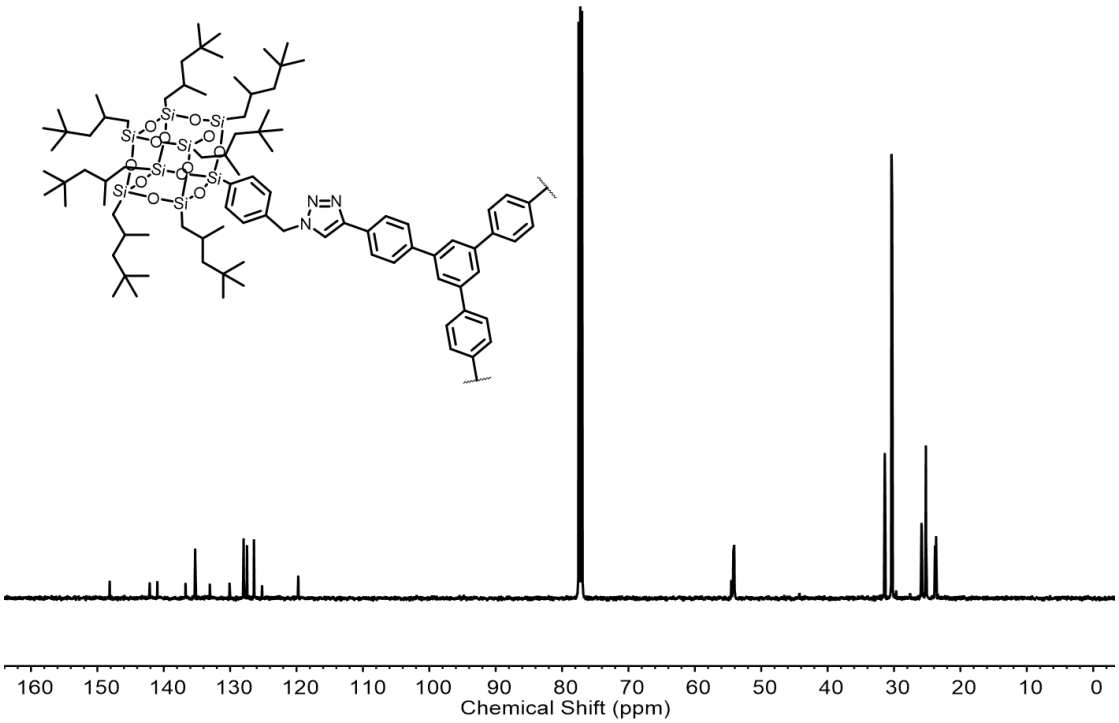

Figure S24. ^{13}C NMR spectra of **M1**.

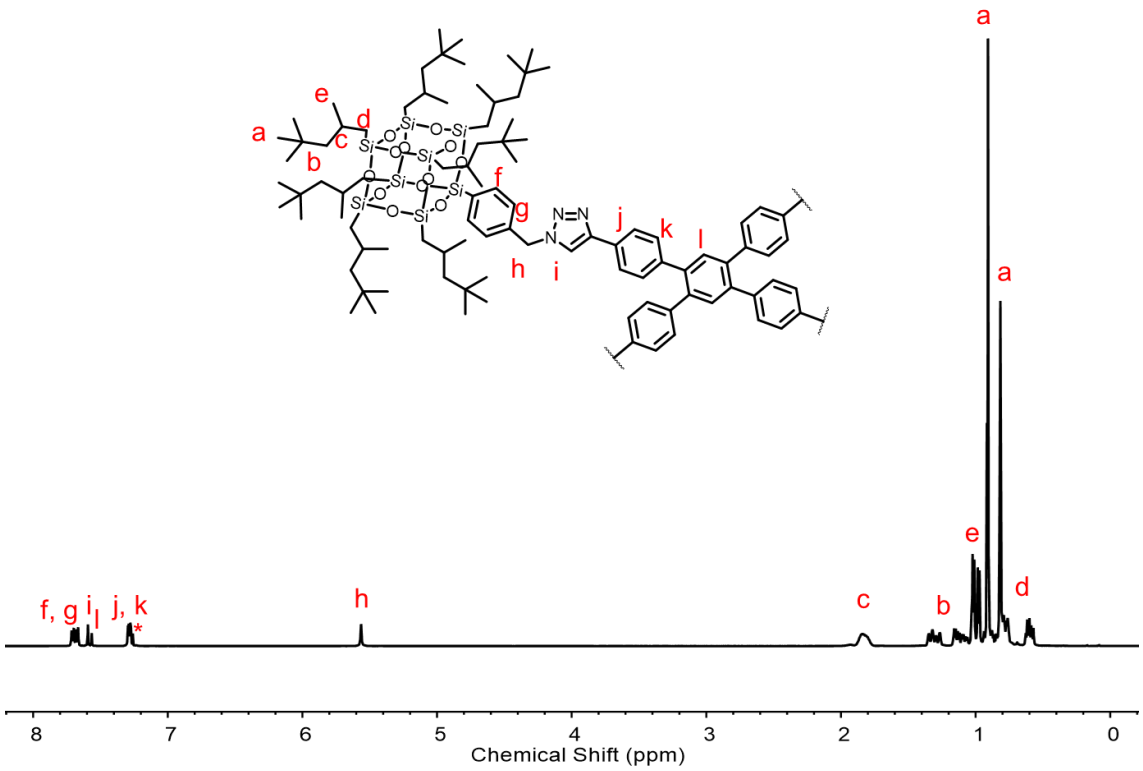

Figure S25. ^{1}H NMR spectra of **M2**.

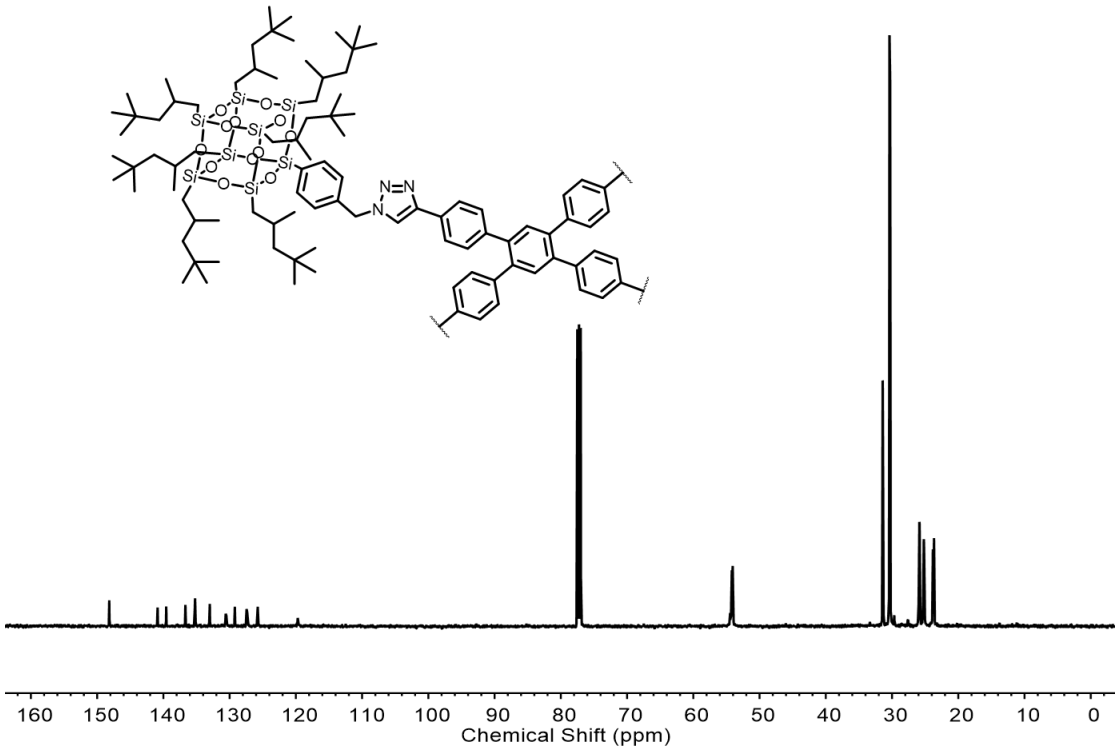

Figure S26. ^{13}C NMR spectra of **M2**.

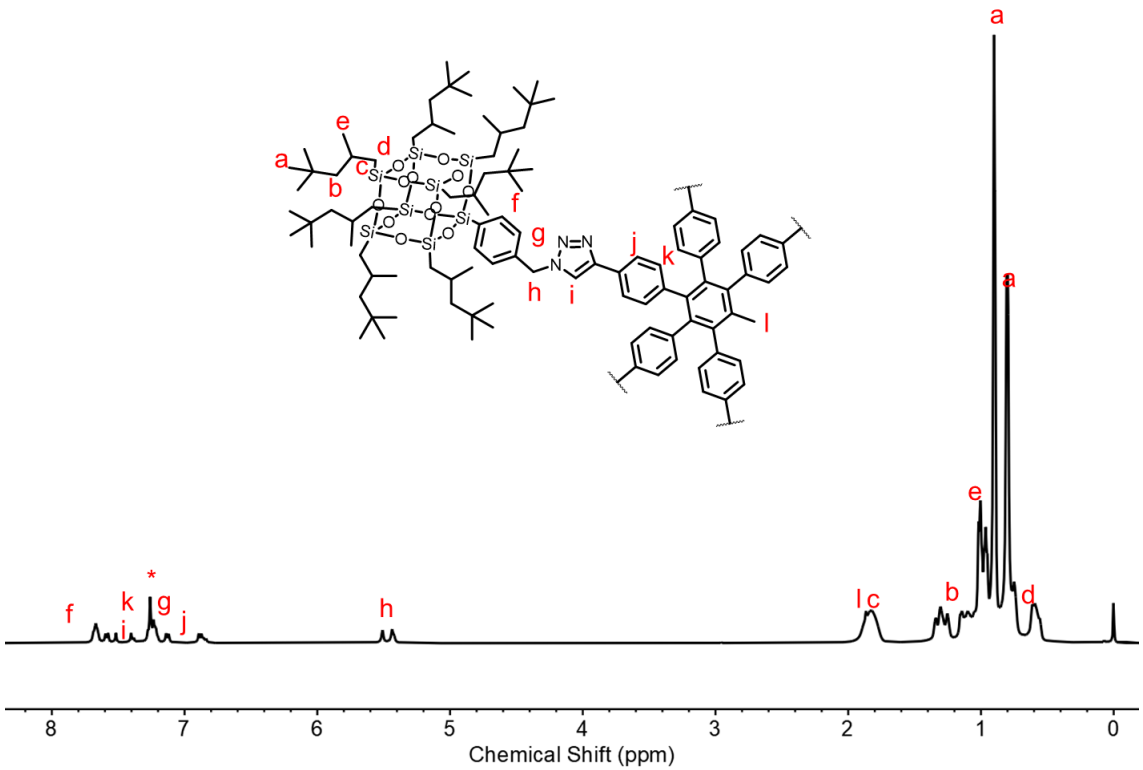

Figure S27. ^{1}H NMR spectra of **M3**.

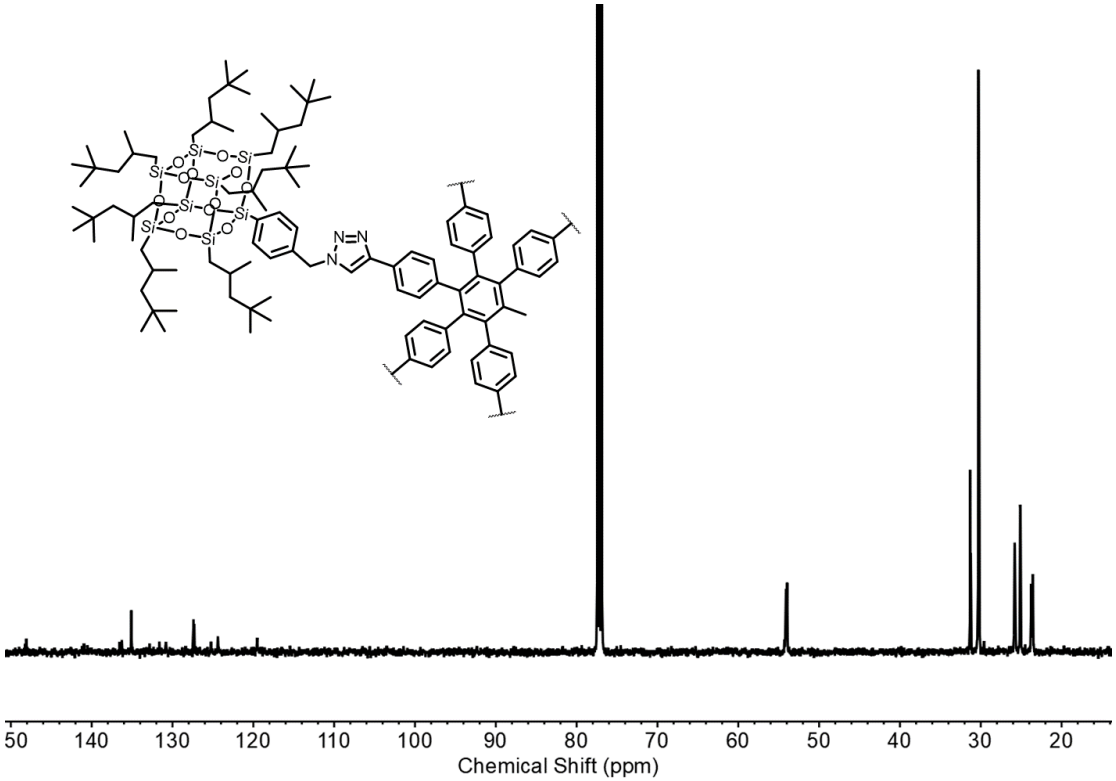

Figure S28. ^{13}C NMR spectra of **M3**.

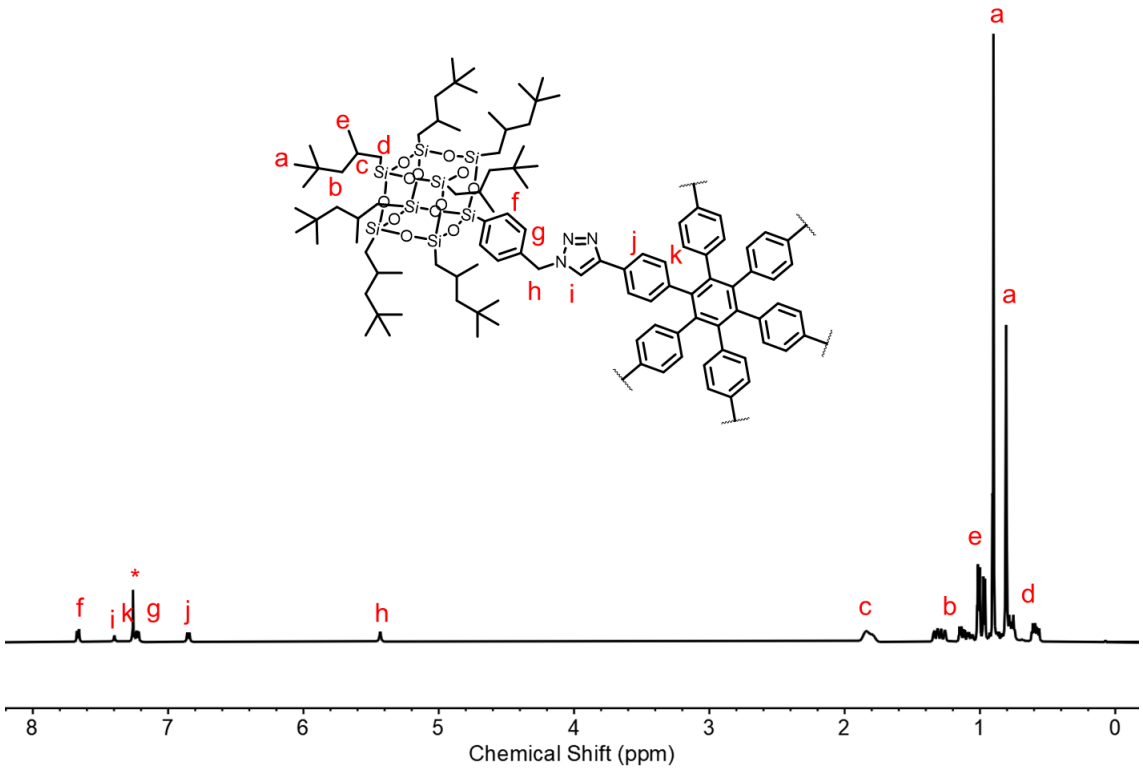

Figure S29. ^{1}H NMR spectra of **M4**.

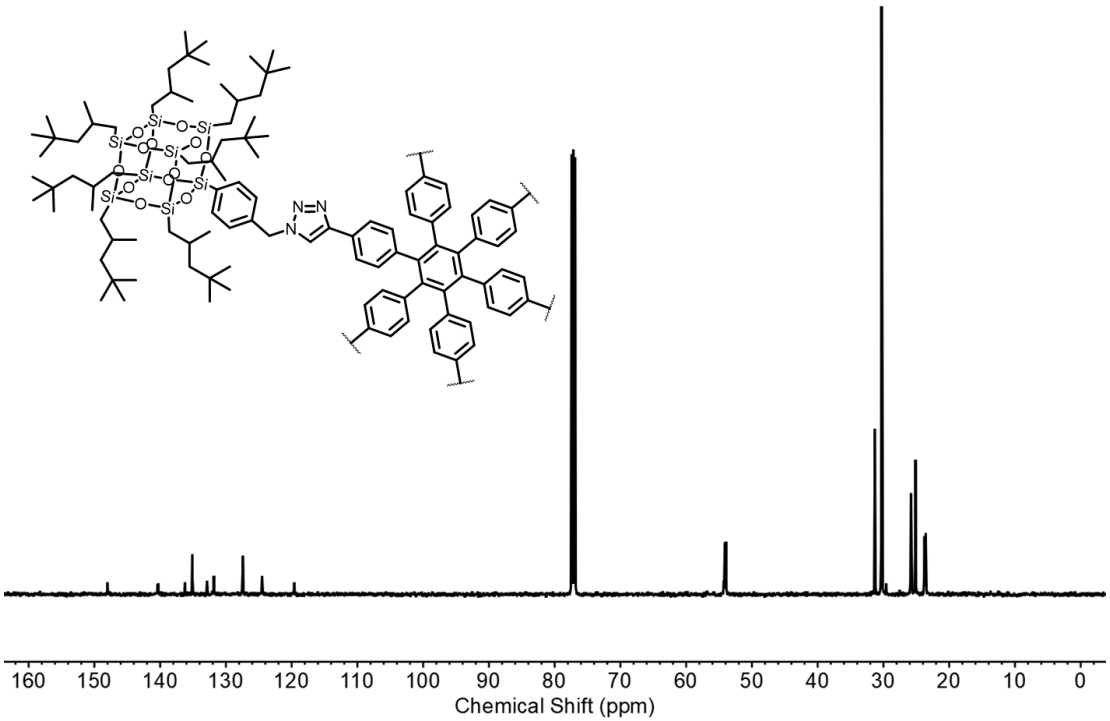

Figure S30. ^{13}C NMR spectra of **M4**.

4. Supplementary Tables

Table S1. FK phases discovered in different material systems.

Material	Year of Identifying FK Phases	Length Scale	Key References
Small-Molecule Crystals	2021	1.2-1.5 nm	[16]
Giant-Molecule superlattices	2015	3.8-12.5 nm	[17-19]
Liquid Foams*	2012	~2.4 mm	[20]
DNA-Grafted Colloidal Crystals	2011	5-650 nm	[21,22]
Nanoparticle Superlattices	2006	3.0-13.5 nm	[23,24]
Metal-Organic Framework*	2004	0.76-6.5 nm	[25-27]
Polymer Melts	2003	9.8-52 nm	[28-30]
Dendron/Dendrimer Assemblies	1997	4.2-12 nm	[31,32]
Natural Opal	1995	240-470 nm	[33]
Mesoporous Materials*	1994	2-10 nm	[34-36]
High-Pressure Compounds	1993	0.1-0.4 nm	[37,38]
Lyotropic Liquid Crystals	1990	5.5-9.2 nm	[39-41]
Microsphere Aggregates	1985	85-1160 nm	[42-44]
Zeolites*	1981	~0.83 nm	[45]
Clathrates*	1951	0.73-1.49 nm	[46-48]
Metals/Metal Alloys	1927	0.2-0.3 nm	[49,50]

*Length scales are estimated by calculating the sizes of spheroidal pores from lattice parameters.

Table S2. List of the 28 (with metallic prototype) + 1 (without metallic prototype) types of Frank-Kasper phases discovered to date (phases identified in the present study are labeled in red).

Number	Phase	Prototype	Space group	Atomic Number	Combination of coordination number (CN) 12/14/15/16	Average CN
1	A_{15}	Cr_3Si	$Pm\bar{3}n$	8	(1, 3, 0, 0)	13.500
2	σ	$Cr_{46}Fe_{54}$	$P4_2/mnm$	30	(5, 8, 2, 0)	13.466
3	H_{comp}	Complex	$Cmmm$	30	(5, 8, 2, 0)	13.466
4	K_{comp}	Complex	$Pmmm$	82	(14, 21, 6, 0)	13.463
5	F_{comp}	Complex	$P6/mmm$	52	(9, 13, 4, 0)	13.461
6	J_{comp}	Complex	$Pmmm$	22	(4, 5, 2, 0)	13.454
7	υ	$Mn_{81.5}Si_{18.5}$	$Immm$	186	(37, 40, 10, 6)	13.440
8	Z	Zr_4Al_3	$P6/mmm$	7	(3, 2, 2, 0)	13.428
9	P	$Mo_{42}Cr_{18}Ni_{40}$	$Pbnm$	56	(6, 5, 2, 1)	13.428
10	δ	MoNi	$P2_12_12_1$	56	(6, 5, 2, 1)	13.428
11	K	$Mn_{77}Fe_4Si_{19}$	$C2$	220	(25, 19, 4, 7)	13.418
12	ϕ	Molecular Pentagon	$Imm2$	54	(13, 8, 2, 4)	13.407
13	R	$Mo_{31}Cr_{51}Co_{18}$	$R\bar{3}$	159	(27, 12, 6, 8)	13.396
14	μ	Mo_6Co_7	$R\bar{3}m$	39	(7, 2, 2, 2)	13.384
15	zra-d	K_7Cs_6	$P6_3/mmc$	26	(7, 2, 2, 2)	13.384
16	pσ	Th_6Cd_7	$Pbam$	26	(7, 2, 2, 2)	13.384
17	M	$Nb_{48}Ni_{39}Al_{13}$	$Pnma$	52	(7, 2, 2, 2)	13.384
18	I	$V_{41}Ni_{36}Si_{23}$	Cc	228	(11, 2, 2, 4)	13.368
19	C	$V_2(Co, Si)_3$	$C2/m$	50	(15, 2, 2, 6)	13.360
20	T	$Mg_{32}(Zn, Al)_{49}$	$Im\bar{3}$	162	(49, 6, 6, 20)	13.358
21	X	$Mn_{45}Co_{40}Si_{15}$	$Pnnm$	74	(23, 2, 2, 10)	13.351
22	mz	Mg_4Zn_7	$C2/m$	110	(35, 2, 2, 16)	13.345
23	6-layers	MgCuNi	$P6_3/mmc$	36	(2, 0, 0, 1)	13.333
24	8-layers	$MgZn_2$+0.03$MgAg_2$	$P6_3/mmc$	48	(2, 0, 0, 1)	13.333
25	9-layers	$MgZn_2$+0.07$MgAg_2$	$R\bar{3}m$	54	(2, 0, 0, 1)	13.333
26	10-layers	$MgZn_2$+0.1$MgAg_2$	$P6_3/mmc$	60	(2, 0, 0, 1)	13.333
27	C_{36}	$MgNi_2$	$P6_3/mmc$	24	(2, 0, 0, 1)	13.333
28	C_{15}	$MgCu_2$	$Fd\bar{3}m$	24	(2, 0, 0, 1)	13.333
29	C_{14}	$MgZn_2$	$P6_3/mmc$	12	(2, 0, 0, 1)	13.333

Table S3. Coordinates of mesoatoms in μ phase (Wyckoff positions are denoted in Figure S6, crystal structure in .cif format is presented in https://doi.org/10.6084/m9.figshare.23497661.v1).

Crystal Structure (Space Group)	**Wyckoff Position**	***x***	***y***	***z***	***IQ***	$\overline{IQ}$
μ phase (*R*-3*m*)	18h	0.16670	0.33340	0.74380	0.7372	0.7617
	6c	0.33333	0.66667	0.50117	0.7695	
	3a	0.33333	0.66667	0.66667	0.7447	
	6c’	0.33333	0.66667	0.21487	0.7887	
	6c’’	0.33333	0.66667	0.31837	0.8092	

Table S4. Coordinates of mesoatoms in ϕ phase (Wyckoff positions are denoted in Figure S7, crystal structure in .cif format is presented in https://doi.org/10.6084/m9.figshare.23497661.v1).

Crystal Structure (Space Group)	**Wyckoff Position**	***x***	***y***	***z***	***IQ***	$\overline{IQ}$
ϕ phase (*Imm*2)	8e	0.25000	0.66954	0.24565	0.7422	0.7485
	4d[a]	0.50000	0.58510	0.09849	0.7348	
	4d[b]	0.50000	0.36558	0.69583	0.7078	
	4d[c]	0.50000	0.08483	0.89294	0.7348	
	4c[a]	0.25000	0.50000	0.95190	0.7314	
	2a[a]	0.50000	0.50000	0.74758	0.6374	
	4d[d]	0.50000	0.79661	0.07651	0.7706	
	4d[e]	0.50000	0.33086	0.44273	0.7691	
	4d[f]	0.50000	0.83081	0.54867	0.7692	
	4c[b]	0.75000	0.00000	0.03963	0.7255	
	4d[g]	0.50000	0.70407	0.91496	0.7820	
	2b	0.00000	0.50000	0.17855	0.8029	
	2a[b]	0.00000	0.00000	0.81278	0.8028	
	4d[h]	0.00000	0.63317	0.79637	0.7730	

Table S5. The *R* values for Jones zones of all FK phases discovered in soft matters.

Phase	$\boldsymbol{R}$	**Deviation from spherical shape** ($\boldsymbol{\delta = |R-1| \times 100\%}$)
A15	0.999	0.1%
σ	0.991	0.9%
μ	1.007	0.7%
ϕ	0.974	2.6%

Table S6. Specifications of simulated system of amorphous melts

Molecule	$N_{molecule}$	N_{atom}	L (nm)
M1	146	99426	10.36068
M2	110	99440	10.38942
M3	88	99440	10.34014
MP	88	99000	10.32711
M4	73	98550	10.32000

$N_{molecule}$: number of giant molecules; N_{atom}: number of atoms; L: side length of simulation box.

Table S7. Observed and calculated peak positions for μ phase formed upon in-situ cooling **MP** melt back to 200 ºC for 3 min. peak positions were calculated using *R*-3*m* space group symmetry with lattice parameters $a = b = 6.992$ nm, $c = 39.55$ nm.

Miller Indices (***h k l***)	q_{obs} ($Å^{-1}$)	q_{calc} ($Å^{-1}$)	**%Residual** $\Delta q/q_{calc} \times 100$
(1 1 0)	0.1797	0.1797	0.00
(1 1 3)	0.1859	0.1859	0.00
(1 0 10)	0.1897	0.1898	-0.05
(0 0 12)	0.1906	0.1906	0.00
(1 1 6)	0.2034	0.2034	0.00
(2 0 -1)	0.2081	0.2081	0.00
(2 0 2)	0.2100	0.2099	0.05
(2 0 -4)	0.2169	0.2170	-0.05
(2 0 5)	0.2222	0.2222	0.00
(1 1 9)	0.2297	0.2297	0.00
(1 0 13)	0.2312	0.2311	0.04
(2 0 -7)	0.2353	0.2354	-0.04
(3 0 0)	0.3115	0.3113	0.06
(2 1 10)	0.3174	0.3172	0.06
(3 0 6), (3 0 -6)	0.3255	0.3256	-0.03
(2 0 -16)	0.3283	0.3281	0.06
(1 0 -20)	0.3340	0.3342	-0.06
(1 1 18)	0.3379	0.3378	0.03
(2 0 17)	0.3411	0.3405	0.18
(2 2 0)	0.3596	0.3595	0.03

Table S8. Observed and calculated peak positions for ϕ phase formed upon in-situ cooling **MP** to 160 °C for 2 hours. Peak positions were calculated using *Imm*2 space group symmetry with lattice parameters a = 6.946 nm, b = 19.010 nm, c = 18.377 nm.

Miller Indices (***h k l***)	q_{obs} ($Å^{-1}$)	q_{calc} ($Å^{-1}$)	**%Residual** $\Delta q/q_{calc}\times 100$
(0 3 3)	0.1421	0.1429	-0.56
(0 4 2)	0.1490	0.1490	0.00
(1 2 3)	0.1526	0.1521	0.33
(0 2 4)	0.1526	0.1523	0.20
(1 4 1)	0.1639	0.1638	0.06
(1 1 4)	0.1681	0.1677	0.24
(0 5 1)	0.1681	0.1688	-0.41
(0 1 5)	0.1747	0.1747	0.00
(2 0 0)	0.1810	0.1809	0.06
(2 1 1)	0.1870	0.1871	-0.05
(1 3 4)	0.1916	0.1920	-0.21
(0 5 3)	0.1946	0.1947	-0.05
(0 3 5)	0.1979	0.1982	-0.15
(0 6 0)	0.1985	0.1983	0.10
(1 5 2)	0.2004	0.2005	-0.05
(2 2 2)	0.2047	0.2045	0.10
(1 2 5)	0.2047	0.2049	-0.10
(2 3 1)	0.2092	0.2091	0.05
(2 1 3)	0.2109	0.2108	0.05
(0 2 6)	0.2162	0.2162	0.00
(1 6 1)	0.2206	0.2206	0.00
(2 4 0)	0.2241	0.2241	0.00
(2 0 4)	0.2269	0.2271	-0.09
(1 1 6)	0.2269	0.2273	-0.18
(2 3 3)	0.2301	0.2306	-0.22
(0 7 1)	0.2341	0.2339	0.09
(2 4 2)	0.2341	0.2343	-0.09
(2 2 4)	0.2362	0.2365	-0.13

(1 6 3)	0.2407	0.2410	-0.12
(0 6 4)	0.2407	0.2412	-0.21
(0 1 7)	0.2423	0.2424	-0.04
(2 5 1)	0.2472	0.2474	-0.08
(2 1 5)	0.2515	0.2515	0.00
(3 3 4)	0.3197	0.3199	-0.06
(1 0 9)	0.3219	0.3218	0.03
(3 5 2)	0.3249	0.3251	-0.06
(2 8 2)	0.3274	0.3276	-0.06
(0 10 0)	0.3306	0.3305	0.03
(0 7 7)	0.3345	0.3335	0.30
(0 8 6)	0.3345	0.3351	-0.18
(0 6 8)	0.3389	0.3386	0.09
(2 5 7), (0 0 10)	0.3433	0.3431	0.06
(0 9 5)	0.3433	0.3434	-0.03
(3 4 5)	0.3474	0.3472	0.06

Table S9. Lattice parameters, micellar radii (R_{sphere}), and average molecular numbers ($\bar{N}$) per mesoatom of mesophases in the present study.

Molecules	***M*w (g/mol)**	**Phase**	**Lattice Parameters***	R_{sphere} **(nm)**	$\bar{N}$
MP	7274.60	ϕ	a=6.706 nm, b=18.704 nm, c=18.007 nm, α=β=γ=90°	2.18	3.63
		μ	a=b=6.756 nm, c=38.647 nm, α=β=90°, γ=120°	2.11	3.40
M1	4402.62	BCC**	a=b=c=4.51 nm, α=β=γ=90°	2.22	6.52
M2	5844.12	BCC	a=b=c=4.23 nm, α=β=γ=90°	2.09	4.08
M3	7299.65	BCC**	a=b=c=4.26 nm, α=β=γ=90°	2.10	3.32
M4	8727.13	BCC	a=b=c=4.33 nm, α=β=γ=90°	2.13	2.93

*All lattice parameters are determined at room temperature, data may slightly vary from the values determined by in-situ experiments (Table S7, S7) due to thermal expansion.

**More than one type of mesoatoms coexist in the BCC-type lattice. Therefore, strictly speaking, the lattice may be CsCl-type or with substitutional defects.

Table S10. Proposed combinations of mesoatoms with different molecular numbers

Phase	**CN**	**Combination of {CN12, CN14, CN15, CN16}**	$\overline{N_{exp}}$	**Wyckoff positions of 3-molecule mesoatoms***	**Wyckoff positions of 4-molecule mesoatoms***	**Wyckoff positions of 5-molecule mesoatoms***	**Wyckoff positions of 6-molecule mesoatoms***	$\overline{N_{calc}}$
μ	13.384	{7, 2, 2, 2}	3.46	3a 18h 6c’	6c	6c’’	\	3.46
ϕ	13.407	{13,8,2,4}	3.63	8e 4d[a] 4d[c] 4d[e] 4d[f] 4c[a] 4c[b]	4d[d] 4d[g] 4d[h]	4d[b] 2b 2a[b]	2a[a]	3.63

*Wyckoff positions of μ and ϕ phases are illustrated in Figure S6 and Figure S7, respectively.

Table S11. Calculation of Gibbs entropy of mesoatom size distribution for ϕ phase

Mesoatom size (i)	**3**	**4**	**5**	**6**
No. of mesoatom in unit cell	32	12	8	2
Frequency	96	48	40	12
$\boldsymbol{p_i}$	0.490	0.245	0.204	0.061
$\boldsymbol{p_i \ln p_i}$	-0.350	-0.345	-0.324	-0.171

5. References and Notes

1 Neese, F. The ORCA program system. *Wiley Interdiscip. Rev. Comput. Mol. Sci.* **2**, 73-78, (2011).

2 Abraham, M. J. *et al.* GROMACS: High performance molecular simulations through multi-level parallelism from laptops to supercomputers. *SoftwareX* **1-2**, 19-25, (2015).

3 Jorgensen, W. L., Maxwell, D. S. & Tirado-Rives, J. Development and Testing of the OPLS All-Atom Force Field on Conformational Energetics and Properties of Organic Liquids. *J. Am. Chem. Soc.* **118**, 11225-11236, (1996).

4 Wilmer, C. E., Kim, K. C. & Snurr, R. Q. An Extended Charge Equilibration Method. *J. Phys. Chem. Lett.* **3**, 2506-2511, (2012).

5 O'Boyle, N. M. *et al.* Open Babel: An open chemical toolbox. *J. Cheminform.* **3**, 33, (2011).

6 Kim, S. A., Jeong, K. J., Yethiraj, A. & Mahanthappa, M. K. Low-symmetry sphere packings of simple surfactant micelles induced by ionic sphericity. *Proc. Natl. Acad. Sci. U. S. A.* **114**, 4072-4077, (2017).

7 Kattirtzi, J. A., Limmer, D. T. & Willard, A. P. Microscopic dynamics of charge separation at the aqueous electrochemical interface. *Proc. Natl. Acad. Sci. U. S. A.* **114**, 13374-13379, (2017).

8 Huang, J. *et al.* Rational Route Toward the Frank–Kasper Z Phase: Effect of Precise Geometrical Tuning on the Supramolecular Assembly of Giant Shape Amphiphiles. *Macromolecules* **54**, 7777-7785, (2021).

9 Qu, H. *et al.* Truncated Face-Rotating Polyhedra Constructed from Pentagonal Pentaphenylpyrrole through Graph Theory. *J. Am. Chem. Soc.* **142**, 16223-16228, (2020).

10 Chen, X. *et al.* Palladium-Catalyzed Reaction of Arylamine and Diarylacetylene: Solvent-Controlled Construction of 2,3-Diarylindoles and Pentaarylpyrroles. *Eur. J. Org. Chem.* **2012**, 4380-4386, (2012).

11 Senesi, A. J. & Lee, B. Small-angle scattering of particle assemblies. *J. Appl. Crystallogr.* **48**, 1172-1182, (2015).

12 Boles, M. A., Engel, M. & Talapin, D. V. Self-Assembly of Colloidal Nanocrystals: From Intricate Structures to Functional Materials. *Chem. Rev.* **116**, 11220-11289, (2016).

13 Lee, S., Leighton, C. & Bates, F. S. Sphericity and symmetry breaking in the formation of Frank-Kasper phases from one component materials. *Proc. Natl. Acad. Sci. U. S. A.* **111**, 17723-17731, (2014).

14 Ziherl, P. & Kamien, R. D. Maximizing Entropy by Minimizing Area: Towards a New Principle of Self-Organization. *J. Phys. Chem. B* **105**, 10147-10158, (2001).

15 Altmann, S. L. *Band Theory of Metals: The Elements*. (Elsevier Science, 2013).

16 Montis, R. *et al.* Complex structures arising from the self-assembly of a simple organic salt. *Nature* **590**, 275-278, (2021).

17 Huang, M. *et al.* Self-assembly. Selective assemblies of giant tetrahedra via precisely controlled positional interactions. *Science* **348**, 424-428, (2015).

18 Jiang, J. *et al.* Modularly Constructed Polyhedral Oligomeric Silsesquioxane-Based Giant

Molecules for Unconventional Nanostructure Fabrication. *ACS Appl. Nano Mater.* **3**, 2952-2958, (2020).

19 Ni, B. *et al.* Facile synthesis and linker guided self-assembly of dendron-like amphiphiles. *Polymer* **167**, 118-121, (2019).

20 Gabbrielli, R., Meagher, A. J., Weaire, D., Brakke, K. A. & Hutzler, S. An experimental realization of the Weaire–Phelan structure in monodisperse liquid foam. *Philos. Mag. Lett.* **92**, 1-6, (2012).

21 Macfarlane, R. J. *et al.* Nanoparticle superlattice engineering with DNA. *Science* **334**, 204-208, (2011).

22 Ducrot, E., He, M., Yi, G. R. & Pine, D. J. Colloidal alloys with preassembled clusters and spheres. *Nat. Mater.* **16**, 652-657, (2017).

23 Shevchenko, E. V., Talapin, D. V., Kotov, N. A., O'Brien, S. & Murray, C. B. Structural diversity in binary nanoparticle superlattices. *Nature* **439**, 55-59, (2006).

24 Wang, D. *et al.* Quantitative 3D real-space analysis of Laves phase supraparticles. *Nat. Commun.* **12**, 3980, (2021).

25 Ferey, G. *et al.* A hybrid solid with giant pores prepared by a combination of targeted chemistry, simulation, and powder diffraction. *Angew. Chem. Int. Ed.* **43**, 6296-6301, (2004).

26 Wang, X. S. *et al.* Syntheses, crystal structures, and luminescent properties of three novel zinc coordination polymers with tetrazolyl ligands. *Inorg. Chem.* **44**, 5278-5285, (2005).

27 Guo, Y.-N. *et al.* Effect of cationic surfactants on structure and morphology of mesostructured MOFs. *RSC Adv.* **2**, (2012).

28 Uddin, M. H. *et al.* Phase Behavior and Microstructure of Poly(oxyethylene)−Poly(dimethylsiloxane) Copolymer Melt. *Macromolecules* **36**, 1261-1271, (2003).

29 Sun, Y. *et al.* Discrete Block Copolymers with Diverse Architectures: Resolving Complex Spherical Phases with One Monomer Resolution. *ACS Cent. Sci.* **6**, 1386-1393, (2020).

30 Xie, S., Lindsay, A. P., Bates, F. S. & Lodge, T. P. Formation of a C15 Laves Phase with a Giant Unit Cell in Salt-Doped A/B/AB Ternary Polymer Blends. *ACS Nano* **14**, 13754-13764, (2020).

31 Hudson, S. D. *et al.* Direct Visualization of Individual Cylindrical and Spherical Supramolecular Dendrimers. *Science* **278**, 449-452, (1997).

32 Cho, B. K., Jain, A., Gruner, S. M. & Wiesner, U. Mesophase structure-mechanical and ionic transport correlations in extended amphiphilic dendrons. *Science* **305**, 1598-1601, (2004).

33 Gauthier, J.-P., Fritsch, E., Aguilar-Reyes, B., Barreau, A. & Lasnier, B. Phase de Laves dans la première opale CT bidisperse. *C. R. - Geosci.* **336**, 187-196, (2004).

34 Huo, Q. *et al.* Generalized synthesis of periodic surfactant/inorganic composite materials. *Nature* **368**, 317-321, (1994).

35 Aubert, T., Ma, K., Tan, K. W. & Wiesner, U. Two-Dimensional Superstructures of Silica

Cages. *Adv. Mater.* **32**, e1908362, (2020).

36 Lin, H. *et al.* Clathrate colloidal crystals. *Science* **355**, 931-935, (2017).

37 Loubeyre, P., Jean-Louis, M., LeToullec, R. & Charon-Gerard, L. High pressure measurements of the He-Ne binary phase diagram at 296 K: Evidence for the stability of a stoichiometric Ne(He)2 solid. *Phys. Rev. Lett.* **70**, 178-181, (1993).

38 Stein, F. & Leineweber, A. Laves phases: a review of their functional and structural applications and an improved fundamental understanding of stability and properties. *J. Mater. Sci.* **56**, 5321-5427, (2020).

39 Baez-Cotto, C. M. & Mahanthappa, M. K. Micellar Mimicry of Intermetallic C14 and C15 Laves Phases by Aqueous Lyotropic Self-Assembly. *ACS Nano* **12**, 3226-3234, (2018).

40 Valentine, C. S., Jayaraman, A., Mahanthappa, M. K. & Walker, L. M. Shear-Modulated Rates of Phase Transitions in Sphere-Forming Diblock Oligomer Lyotropic Liquid Crystals. *ACS Macro Lett.* **10**, 538-544, (2021).

41 Seddon, J. M., Bartle, E. A. & Mingins, J. Inverse cubic liquid-crystalline phases of phospholipids and related lyotropic systems. *Journal of Physics: Condensed Matter* **2**, SA285-SA290, (1990).

42 Yoshimura, S. & Hachisu, S. Order Formation in Binary-Mixtures of Monodisperse Latexes. *J Phys-Paris* **46**, 115-126, (1985).

43 Okubo, T. Alloy structures in binary mixtures of highly deionized colloids at sedimentation equilibrium. *J. Chem. Phys.* **93**, 8276-8283, (1990).

44 Hynninen, A. P., Christova, C. G., van Roij, R., van Blaaderen, A. & Dijkstra, M. Prediction and observation of crystal structures of oppositely charged colloids. *Phys. Rev. Lett.* **96**, 138308, (2006).

45 Schlenker, J. L. *et al.* Crystal structure of a synthetic high silica zeolite—ZSM-39. *Nature* **294**, 340-342, (1981).

46 Stackelberg, M. v. & Müller, H. R. On the Structure of Gas Hydrates. *J. Chem. Phys.* **19**, 1319-1320, (1951).

47 Dyadin, Y. A. & Udachin, K. A. Clathrate polyhydrates of peralkylonium salts and their analogs. *Journal of Structural Chemistry* **28**, 394-432, (1987).

48 Matsumoto, M. & Tanaka, H. On the structure selectivity of clathrate hydrates. *J. Phys. Chem. B* **115**, 8257-8265, (2011).

49 E. C. Bain, W. E. G. An introduction to the iron-chromium-nickel alloys. *Trans. AIME,* **75**, 166-211, (1927).

50 Rahm, M., Hoffmann, R. & Ashcroft, N. W. Atomic and Ionic Radii of Elements 1-96. *Chemistry* **22**, 14625-14632, (2016).